OBSERVATION AND ANALYSIS OF THE CIRCULATION OFF THE NORTHWEST COAST OF GREENLAND

by

Lauren M. Brown

A thesis submitted to the Faculty of the University of Delaware in partial fulfillment of the requirements for the degree of Master of Science in Marine Studies

Summer 2011

OBSERVATION AND ANALYSIS OF THE CIRCULATION OFF THE NORTHWEST COAST OF GREENLAND

by

Lauren M. Brown

Approved: ____
Andreas K. Münchow, Ph.D.
Professor in charge of thesis on behalf of the Advisory Committee

Approved: ____
Charles E. Epifanio, Ph.D.
Director of the School of Marine Science and Policy

Approved: ____
Nancy M. Targett, Ph.D.
Dean of the College of Earth, Ocean, and Environment

Approved: ____
Charles G. Riordan, Ph.D.
Vice Provost for Graduate and Professional Education

ACKNOWLEDGEMENTS

I would like to express a great deal of gratitude to my advisor, Dr. Andreas Münchow, for his guidance, never-ending patience, and continuous encouragement during the course of my graduate work. I would also like to thank my committee members, Dr. Helga Huntley and Dr. Pablo Huq, for their help and support. I am grateful for the opportunity to work with such inspiring scientists.

My fellow graduate students and colleagues made this a truly memorable experience. I would like to thank Melissa, Berit, Ana, Phil, Neil, James, Zack, Felipe, Joseph, Entin, Chris, and others past and present for their sense of humor and friendship. Thanks also to my graduate school professors for their dedication and inspiration.

I would not be where I am today without my parents, Melvin and Linda, and my brother, Michael. To my family, I am eternally grateful for the love and support you have given me over the years. I would not have made it without you. I hope I can always be there for you the way you have been there for me. Also, to Kristin and Christine, I am truly lucky to have friends like you.

TABLE OF CONTENTS

LIST OF FIGURES

LIST OF TABLES

ABSTRACT

During the months of July and August in 2003, data were collected aboard the USCGC *Healy* from a shipboard acoustic Doppler current profiler (ADCP) and several conductivity-temperature-depth (CTD) stations as a part of the Canadian Archipelago Throughflow Study between Greenland and Ellesmere Island. This study details findings specifically within an area located south of Smith Sound, near the coast of Thule, Greenland.

The West Greenland Current (WGC) carries relatively warm, saline water north into Baffin Bay through Davis Strait. Bourke et al. (1989) suggest that while the majority of the current follows the 500 m isobath and turns cyclonically in northern Baffin Bay, an indeterminate amount continues into the southern part of Smith Sound. Hydrographic and velocity data are used to verify the existence of the WGC in the study area.

A synoptic, snapshot view of velocity and hydrography fields along the northwestern coast of Greenland is analyzed. After removal of the dominant tidal signal from the measured velocity data, volume and freshwater fluxes through the sections are calculated. In addition, vertical velocity shear is determined using the thermal wind balance and measured density fields. Geostrophic velocity calculations are used to find volume flux and this is compared to the volume flux found using measured

ADCP velocity data to further examine the nature of the flow through this region.

Furthermore, a buoyancy-driven coastal current is observed that flows in the direction of Kelvin wave propagation. This coastal current is characterized by maximum velocities greater than 30 cm s^{-1} and is observed at all latitudes examined in this study. Salinity gradients across the section and throughout the water column suggest that freshwater runoff from Greenland is the source of the current.

Chapter 1

INTRODUCTION

The Canadian Arctic Archipelago consists of many narrow straits, as seen in Figure 1.1. Few studies exist for much of the region and long-term data are sparse due to the difficulty of conducting research in this harsh environment. Nares Strait connects the Lincoln Sea and Arctic Ocean north of Greenland to Baffin Bay at the southern end via Smith Sound. Arctic Ocean water also enters Baffin Bay through Jones and Lancaster Sounds and discharges almost entirely through Davis Strait to the south (Rudels, 1986). This water eventually propagates further south into the Labrador Sea and becomes part of the Labrador Current (Melling et al., 2008).

On the eastern side of Davis Strait, the West Greenland Current (hereafter WGC) carries relatively warm and saline water north into Baffin Bay (Rudels, 1986). Bourke et al. (1989) state that the majority of the WGC follows the 500 m isobath and turns cyclonically past Smith Sound to the western side of Baffin Bay. It is thought, however, that an indeterminate amount of this current continues north along the west coast of Greenland and enters the southern part of Smith Sound (Bourke et al., 1989; Melling et al., 2001; Münchow et al., 2007). To date, little is known about the WGC in northern Baffin Bay from direct observation, in part because it is difficult to reach this region. The volume, heat, and freshwater flux

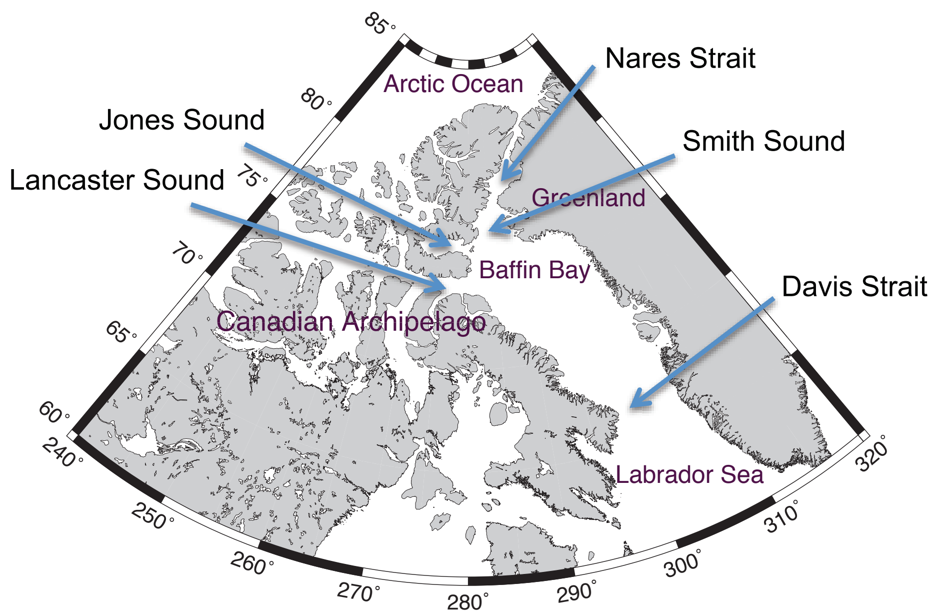

Figure 1.1: A map of the region of interest. Smith Sound is located just north of Baffin Bay and Nares Strait connects Baffin Bay with the Arctic Ocean. Davis Strait is located at the Southern end of Baffin Bay.

of this northern extension of the West Greenland Current onto the shelf areas to the north of 76°N latitude are uncertain. This study provides a first estimate of volume and freshwater fluxes as well as the vertical and horizontal structure of the associated coastal flows near Thule, Greenland.

Thule is located on the northwestern coast of Greenland at about 76.5°N, in northern Baffin Bay, just south of Smith Sound. A detailed map of the region is shown in Figure 1.2. This thesis will demonstrate the existence of a branch of the WGC that propagates along the coast and reaches this latitude. In addition, the runoff and meltwater generated by ice melt on Greenland during the summer months may contribute to a buoyant surface current observed along the coast, driven by across-shore density and baroclinic pressure gradients.

Bacon et al. (2002) present dynamically similar results from a survey of the coastal circulation off Cape Farewell at the southern tip of Greenland and provide an example of the type of flow examined in the present study. Analyzing conductivity-temperature-depth (CTD), acoustic Doppler current profiler (ADCP), and thermosalinograph data, Bacon et al. (2002) discovered a coastal trapped flow driven primarily by the runoff of meltwater from Greenland. The current is approximately 15 km wide and 100 m deep with surface speeds of approximately 1 m s^{-1}. The authors conclude that decreases in salinity, both toward the shore and from the bottom to the surface, indicate that the source of the freshwater is from Greenland. Furthermore, because the data were collected during the summer, meltwater runoff is likely the primary cause of the East Greenland Coastal Current observed in their analysis (Bacon et al., 2002). Buoyancy-driven currents have a significant role in

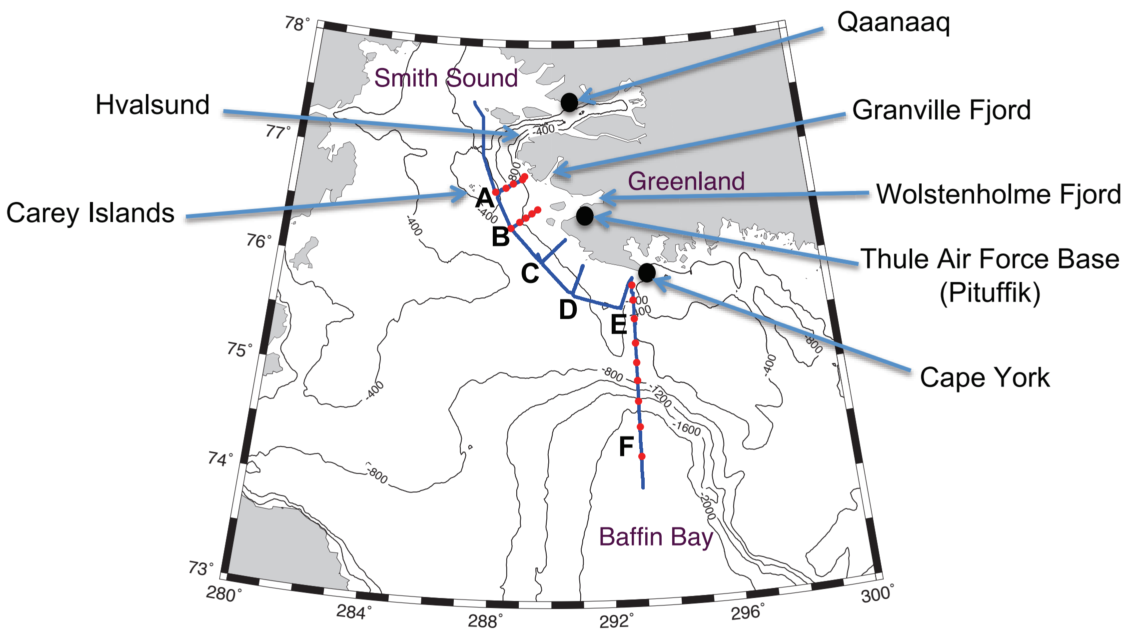

Figure 1.2: A map of the area near Thule, Greenland. The map indicates the ship-track and ADCP data locations (blue lines), and the location of CTD profiles (red symbols). Across-shelf sections are labeled A-F.

freshwater fluxes in the region. One of the goals of this study is to demonstrate that a similar coastal current exists more than 1000 km to the north along the western coast of Greenland.

Melling et al. (2001) discuss the general circulation in northern Baffin Bay and Smith Sound as illustrated in Figure 1.3, using moorings indicated by labeled circles. They find that a fraction of the warm WGC water enters northern Baffin Bay from the southeast and follows the 400 m isobath into the region of the present study (near mooring site S1 in Figure 1.3). Just north of this area, the current splits with one branch curving into Hvalsund to the north and the other branch flowing northwest past the Carey Islands. The former doubles back and carries warm water southward at depth. Melling et al. (2001) show that this deep branch then circulates anti-cyclonically around the Carey Islands. A shallower part of this branch moves westward out of Hvalsund and joins the warm flow that is traceable to 78°N (Melling et al., 2001). The present study describes circulation that is consistent with the analysis of Melling et al. (2001) and demonstrates that the temperature and salinity signature of the WGC is indeed present along the northwest coast of Greenland between latitudes 75.5° and 76.5°N during the summer of 2003.

In Chapter 2, details and descriptions of the instruments and data collected during a 42 hour survey off the coast of Greenland in the summer of 2003 are presented. In Chapter 3, two independent methods are utilized to remove the dominant tidal signals from the velocity observations: the method of least squares (Münchow, 2000) and the barotropic tidal model of Padman and Erofeeva (2004). In Chapters 4 and 5, hydrographic data and sub-tidal velocity fields are examined to identify

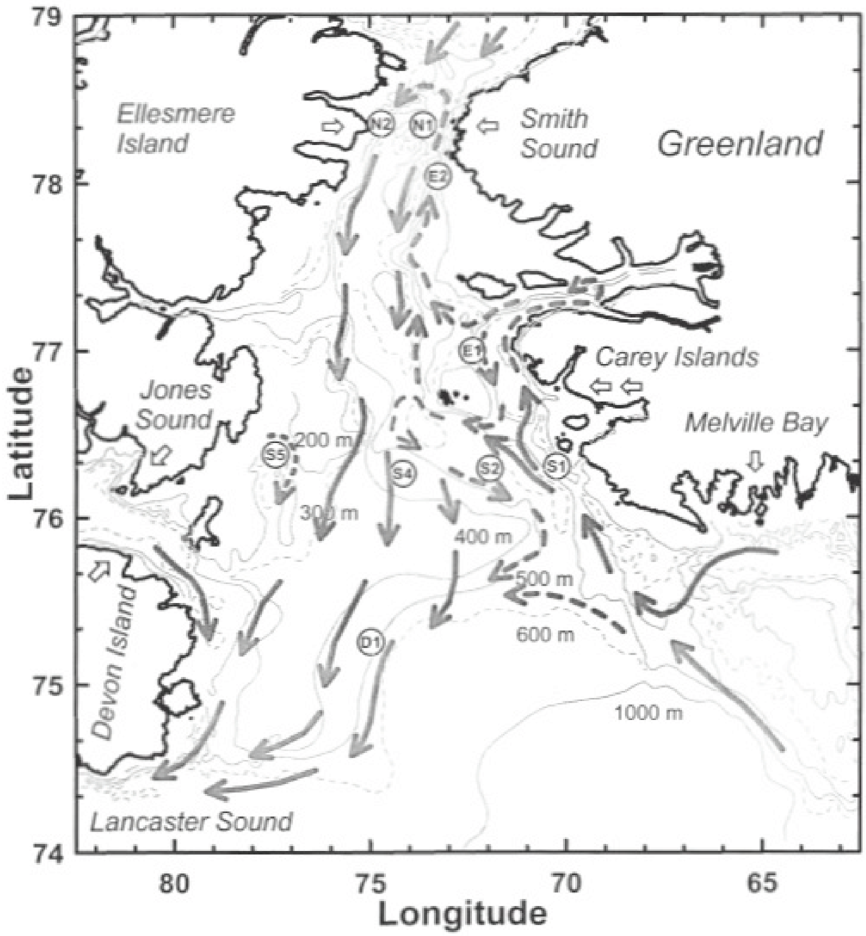

Figure 1.3: This cartoon gives an overview of the general circulation in northern Baffin Bay and Smith Sound. Solid arrows represent motion throughout the water column while dashed arrows represent flow at depth. Labeled circles indicate mooring sites used in the study by Melling et al., 2001. *Source*: Melling et al., 2001.

significant features in the density and flow fields, respectively. Chapter 6 is a first look at the effects of wind fields and internal friction, and Chapter 7 provides a summary discussion.

Chapter 2

STUDY AREA AND DATA SOURCES

2.1 Study Area

During the months of July and August in 2003, the USCGC *Healy* voyaged to Baffin Bay and north into Nares Strait as part of the Canadian Archipelago Through-flow Study (CATS). The project combined scientists and experiments ranging from physical and chemical oceanography to biology and geology. Available equipment included an ADCP, CTD and rosette, multibeam swath mapping system, thermosalinograph, and meteorological sensors. The data discussed herein were collected between 67° and 73°W and 75° and 78°N. This area is situated on the west coast of Greenland near the United States Air Force Base at Thule. Figure 1.2 shows the study area and survey tracks.

Seasonal ice coverage characterizes the coastal region west of Thule. The Moderate Resolution Imaging Spectroradiometer (MODIS) image in Figure 2.1 is representative of the conditions in Baffin Bay during the time of the expedition. The dominant winds were southerly throughout the duration of the expedition and were typically 20 knots or greater. The bathymetry of the region is dominated by a broad, sloping shelf with a deep channel running parallel to the coastline that turns east into Hvalsund at approximately 77°N. The dynamics are further complicated

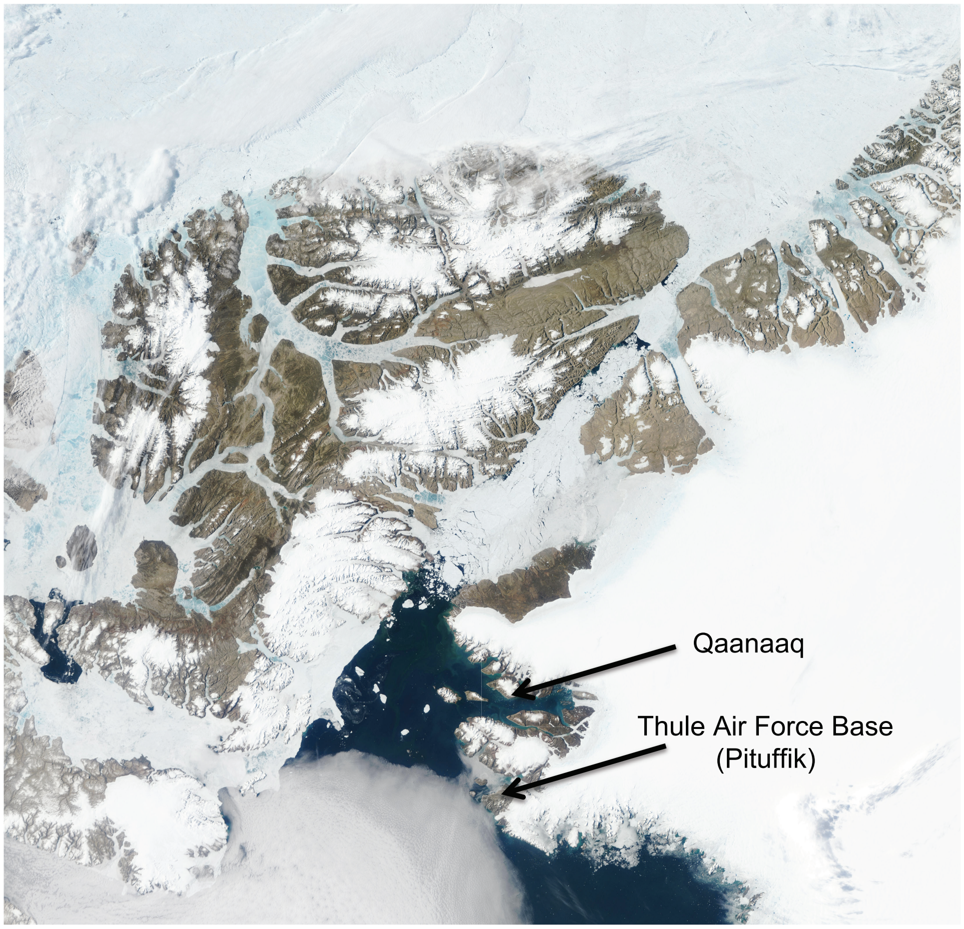

Figure 2.1: An image from MODIS during July 2003 of northern Baffin Bay and Nares Strait. Blue areas indicate open water and brown is land. White areas are ice and grey areas are clouds. *Source*: NASA.

by the Carey Islands just west of Thule at 76.67°N.

2.2 Data Sources and Methods

For 42 hours, the ship was maneuvered to obtain several across-shelf and along-shelf sections. The five sections perpendicular to the coastline are labeled A through E from north to south, as in Figure 1.2. Each of sections A through D include a landward and a seaward track and the data along these tracks were averaged into a single section and binned into 2 km wide segments after removing the tidal signal. The amount of time it takes to survey the desired area and to complete CTD casts, as well as the number and spacing of the casts (spatial and temporal resolution), are important considerations to ensure a synoptic view of the data set. The sections extend across the shelf to more than 35 km offshore between 75.5°N and 77°N. There is also a 220 km transect extending south from Cape York into the center of Baffin Bay (labeled Section F in Figure 1.2).

This study analyzes ADCP, CTD, and wind data obtained along these sections. The *Healy* is equipped with a 75 kHz, vessel-mounted ADCP that estimates the velocity vector using acoustic signals backscattered by organisms such as zooplankton in the water column[1]. Data processing includes the conversion from beam into earth co-ordinates, using heading, pitch, and roll data from an AshTech GPS receiver. The removal of ship motion is determined either from a separate bottom-tracking ADCP pulse or from a Trimble p-code GPS system. Processing also includes single ping data screening prior to averaging over 2 minutes along the ship track (for further details on processing, see Münchow et al., 2006; 2007). In this study, data with less than 50% good pings (percentage of pings that exceed the signal-to-noise threshold) within a 2-minute averaging window and error velocity with values greater than 10 cm s^{-1} were removed. Error velocity results from the comparison of two independent measurements of the vertical velocity made from the 4-beam configuration of the ADCP.

[1] For more information, see *http://www.rdinstruments.com/*.

Acoustic velocity data are recorded and averaged into 15 m depth bins except for the top 33 m, where ship draft and transducer ring down produce too much noise. To fill in the missing areas, ADCP data from 33 m to 78 m below the surface were extrapolated to the surface using a linear regression technique, assuming a constant shear layer (see Figure 2.2). Data from the lowest 15% of the water column were discarded because of acoustic side lobe interference near the bottom. All velocities were decomposed into across-shelf (u) and along-shelf (v) components. In the cross-sectional velocity figures used in this thesis, the x-axis represents distance in km from the west end of the section moving toward the coast.

In addition to the ADCP measurements, 19 CTD casts were collected along sections A, B, and F (see Figure 1.2) using a Sea Bird Electronics SBE 9+ system to measure conductivity, temperature, and depth. From these, salinity and density were calculated. Salinity measurements are accurate to ± 0.002 psu. Additional details on processing techniques can be found in Münchow et al. (2006).

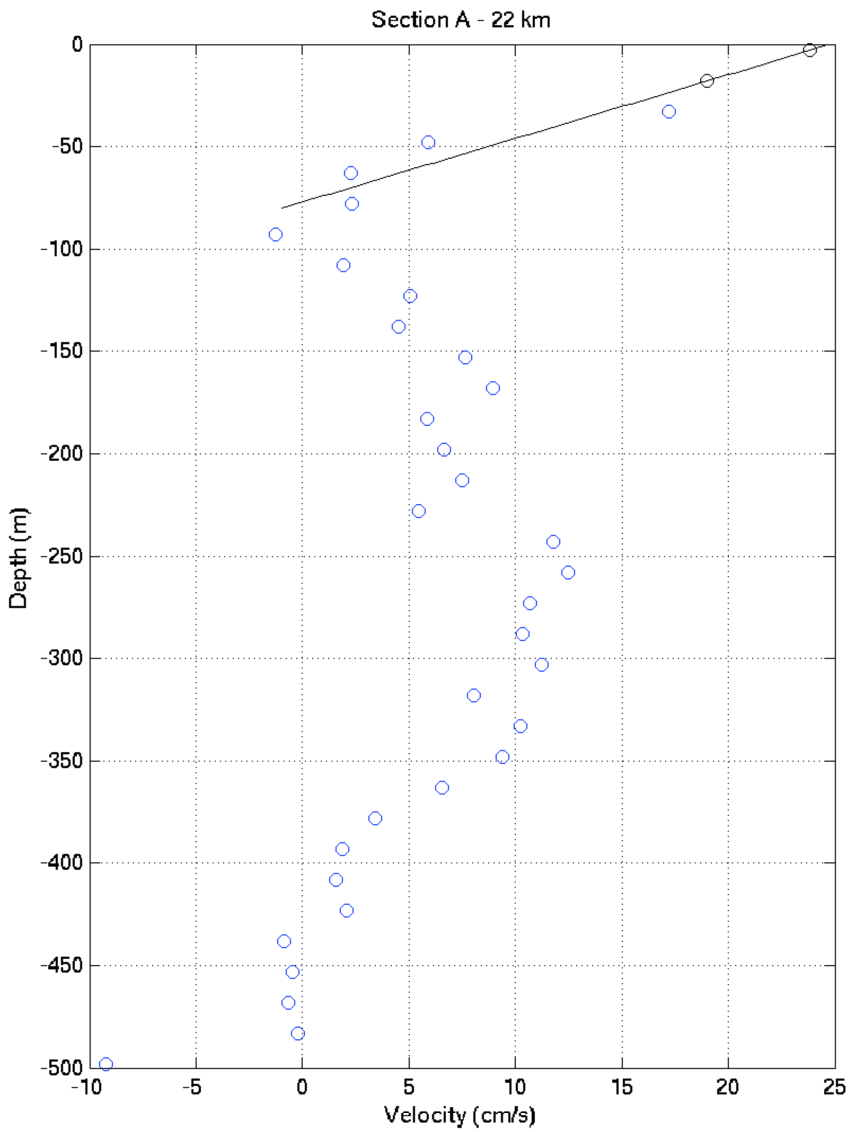

Figure 2.2: This graphic illustrates the linear extrapolation method used to obtain data near the surface. The magnitudes of the measured ADCP velocities are indicated by blue symbols and the extrapolated values at 18 m and 3 m depth are indicated by black symbols.

Chapter 3

TIDES

Local ocean currents are influenced by many factors including tides, weather conditions, geometry of the coastline, bottom topography, and estuarine and glacial runoff. In addition to these influences, currents also vary with longer periodicities including seasonal fluctuations; however, the present data set is restricted to much shorter time scales. Figure 3.1 depicts the depth-averaged velocity time series for the 42 hour data set used in this study. It represents both the tidal and the sub-tidal components of flow. The series begins at the southern end of the study area in Baffin Bay.

Sub-tidal currents and fluxes are successfully revealed only after the identification and removal of the tidal signal at different frequencies. Shallow coastal regions have a different response to tidal forcing than open basin or open ocean regions (Pond and Pickard, 1983). Tides in coastal areas can be heavily influenced by the geometry of the coastline and bottom topography. The diurnal (M_2) and semi-diurnal (K_1) periodicities are the dominant signals in this data set. Tides and the associated constituents vary spatially and temporally as: $\vec{u}_{tide} = \vec{u}_{tide}(x, y, z, t)$.

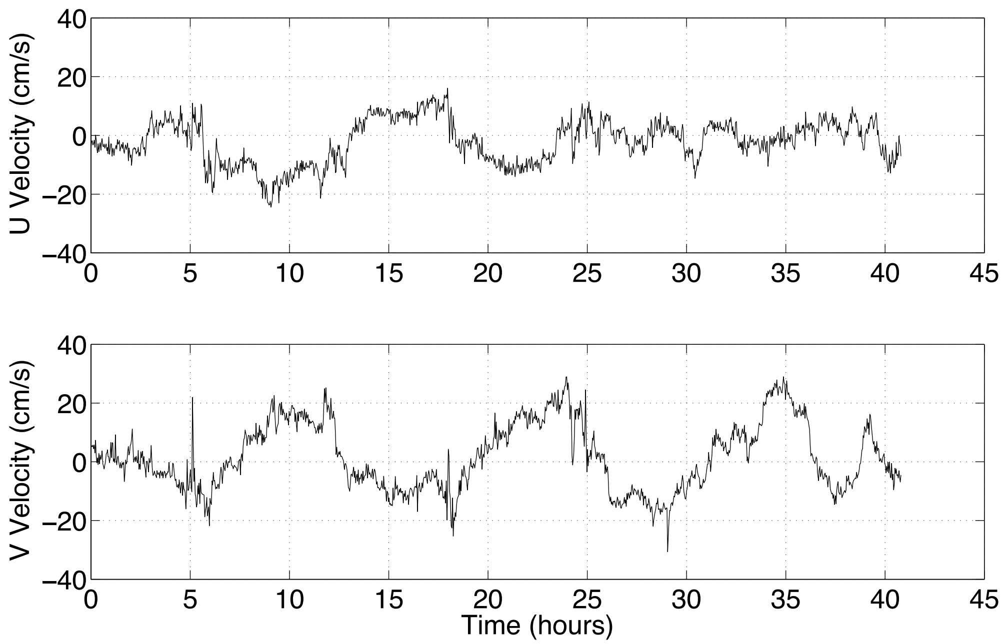

Figure 3.1: This graphic illustrates the depth-averaged velocity time series for the across-shelf (u) and along-shelf components (v). The series begins at the southern end of the study area.

3.1 Harmonic Analysis

As a first estimate of the tidal signal, spatial variability is neglected. The depth-averaged tidal velocity is expressed as the sum of two harmonic components using semi-diurnal and diurnal periodicities. The tidal velocity components (u and v) are empirically modeled by:

$$u = A\sin(\omega_k t) + B\cos(\omega_k t) \tag{3.1}$$

$$v = C\sin(\omega_k t) + D\cos(\omega_k t) \tag{3.2}$$

where amplitudes A, B, C and D are constants determined by least squares fitting (Simpson et al., 1990), ω_k is the known frequency of the semi-diurnal and diurnal tidal constituents, and t is time. Two distinct frequencies are used for the M_2 and the K_1 constituents. This method is explained in detail by Münchow (2000). Figure 3.2 depicts the result of this preliminary tidal analysis superimposed on the depth-averaged ADCP velocity. A comparison of the velocity and fitted tide indicates that the M_2 and K_1 periodicities largely represent the tidal signal in this case, masking the sub-tidal currents.

Ellipse parameters are an effective way to summarize tidal current characteristics. Four parameters (semimajor and semiminor axes, orientation, and phase) can be expressed in terms of the amplitudes A, B, C, and D and were calculated for the M_2 and K_1 constituents. The semimajor axis is representative of the maximum tidal current velocity. The orientation is the angle between east (or the x-axis) and the semimajor axis; the phase is the angle that corresponds to the time of the maximum velocity. The sign of the semiminor axis indicates the direction of rotation.

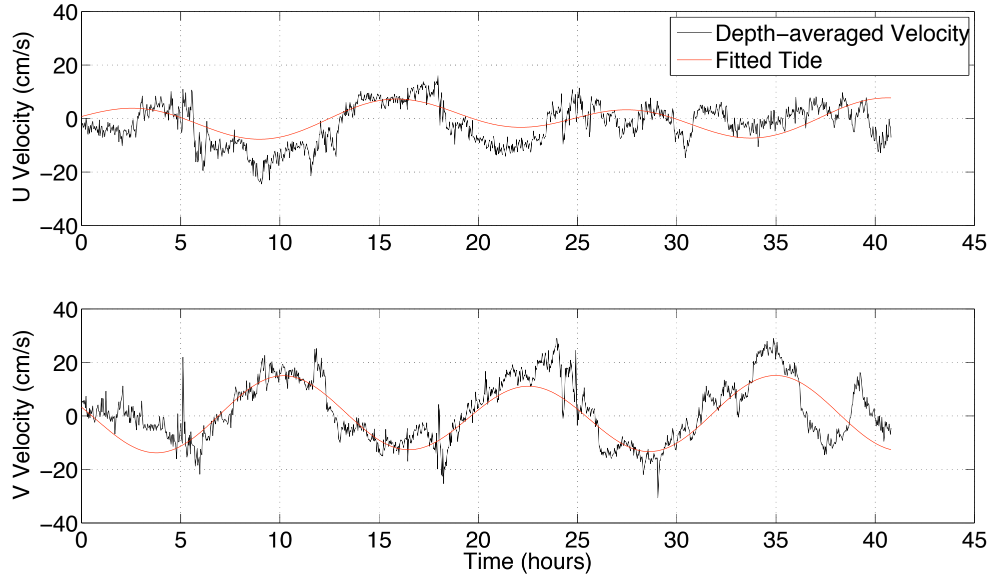

Figure 3.2: This graphic illustrates the depth-averaged velocity (black line) as well as the fitted harmonic tidal signal (red line) using the M_2 and K_1 constituents.

When the semiminor axis is negative, rotation is clockwise. In Figures 3.3 and 3.4 the tidal ellipses for the first estimate of spatially constant tides can be seen. The M_2 ellipse is aligned parallel with the shoreline, while the K_1 ellipse is aligned at an angle to the shoreline. The semimajor axis of the M_2 tidal constituent is approximately 14 cm s^{-1} while the semimajor axis of the K_1 constituent is approximately 3.1 cm s^{-1}, indicating the dominance of the semi-diurnal tide.

In order to refine the tidal estimate, the vertical variation of the tidal signal is examined by fitting tidal currents at each 15 m depth level. Retaining the assumption of no variation horizontally, tidal currents vary as: $\vec{u}_{tide} = \vec{u}_{tide}(z,t)$. Ellipse parameters are calculated with depth and reveal that the tidal signal is primarily barotropic, meaning that there is little vertical variation of the tides. Figure 3.5

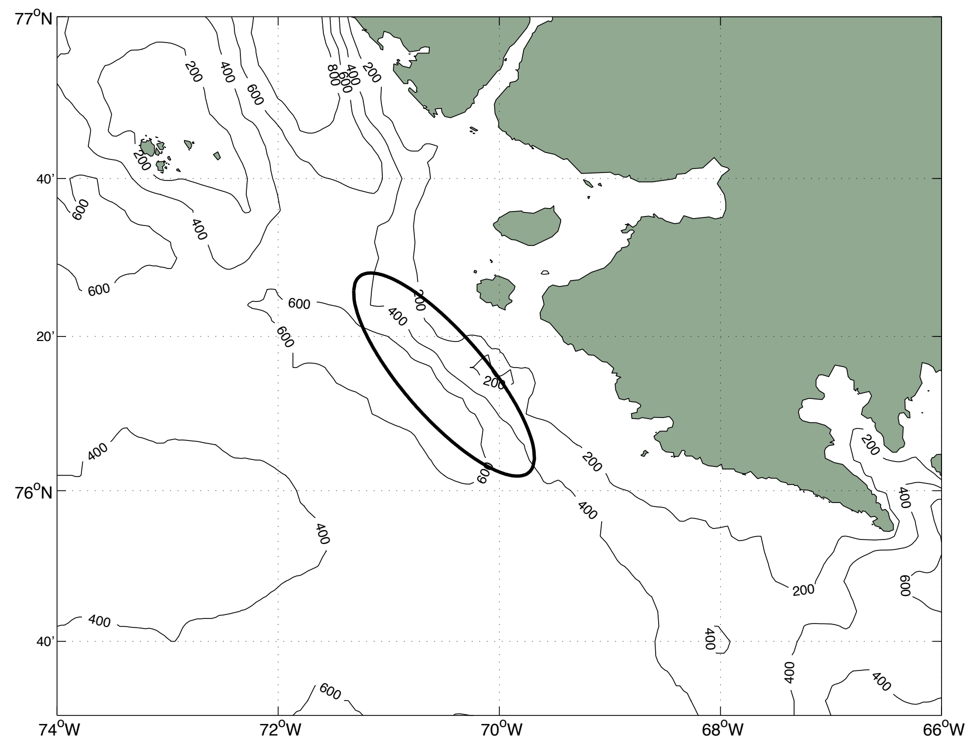

Figure 3.3: Tidal ellipse for the M_2 constituent of the spatially constant tide estimate.

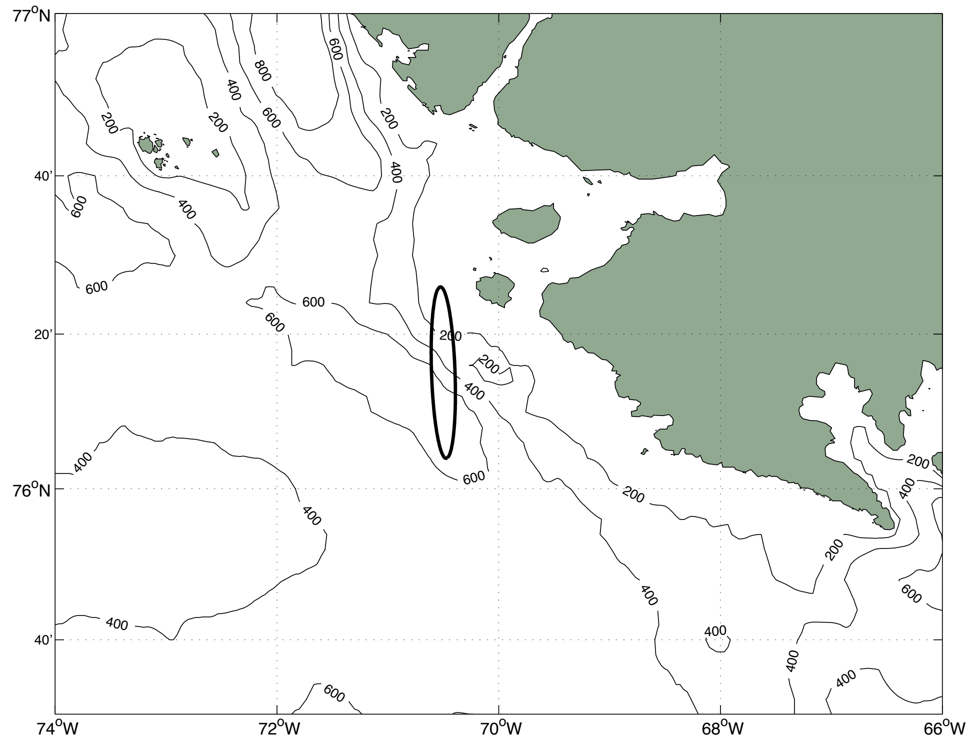

Figure 3.4: Tidal ellipse for the K_1 constituent of the spatially constant tide estimate.

shows the dependence of the ellipse parameters with depth. The M_2 semimajor axis varies between 12 and 17 cm s^{-1} and the K_1 semimajor axis varies between 2 and 6 cm s^{-1}. The semiminor axis is small compared to the semimajor axis. The phase and orientation of the M_2 tide also indicate little variation in the vertical. However, the K_1 orientation does show some variation with depth. The phase of the K_1 tide shifts by about 180° at approximately 130 m depth. There is also a phase shift of about 90° between 230 m and 290 m depth. Shifts in the vertical could be the result of rapid shifts in the density field and stratification at those locations.

In order to refine our tidal prediction further, the data were separated into a near-shore regime and an offshore regime including the continental slope by treating velocity data inshore of the 250 m isobath separately from those data collected in water deeper than 250 m. Thus, tidal currents vary as a function of horizontal and vertical space as well as time. Ellipse parameters for data outside the 250 m isobath are illustrated in Figure 3.6 and parameters for data inside the 250 m isobath are in Figure 3.7.

Offshore of the 250 m isobath, there is little variation in the vertical representation of the semimajor and semiminor axes of both the semi-diurnal and diurnal tides. The M_2 current has a maximum of 18 cm s^{-1}, while the K_1 constituent reaches 5 cm s^{-1}. Similarly, we find very little variation vertically in phase and orientation for the M_2 constituent. However, the K_1 constituent does exhibit some vertical variation in both phase and orientation. We find an approximate 90° phase shift at approximately 250 m depth. We also find an approximate 60° orientation change at the same depth for the K_1 major axis. Thus, the fixed-phase tidal currents at any

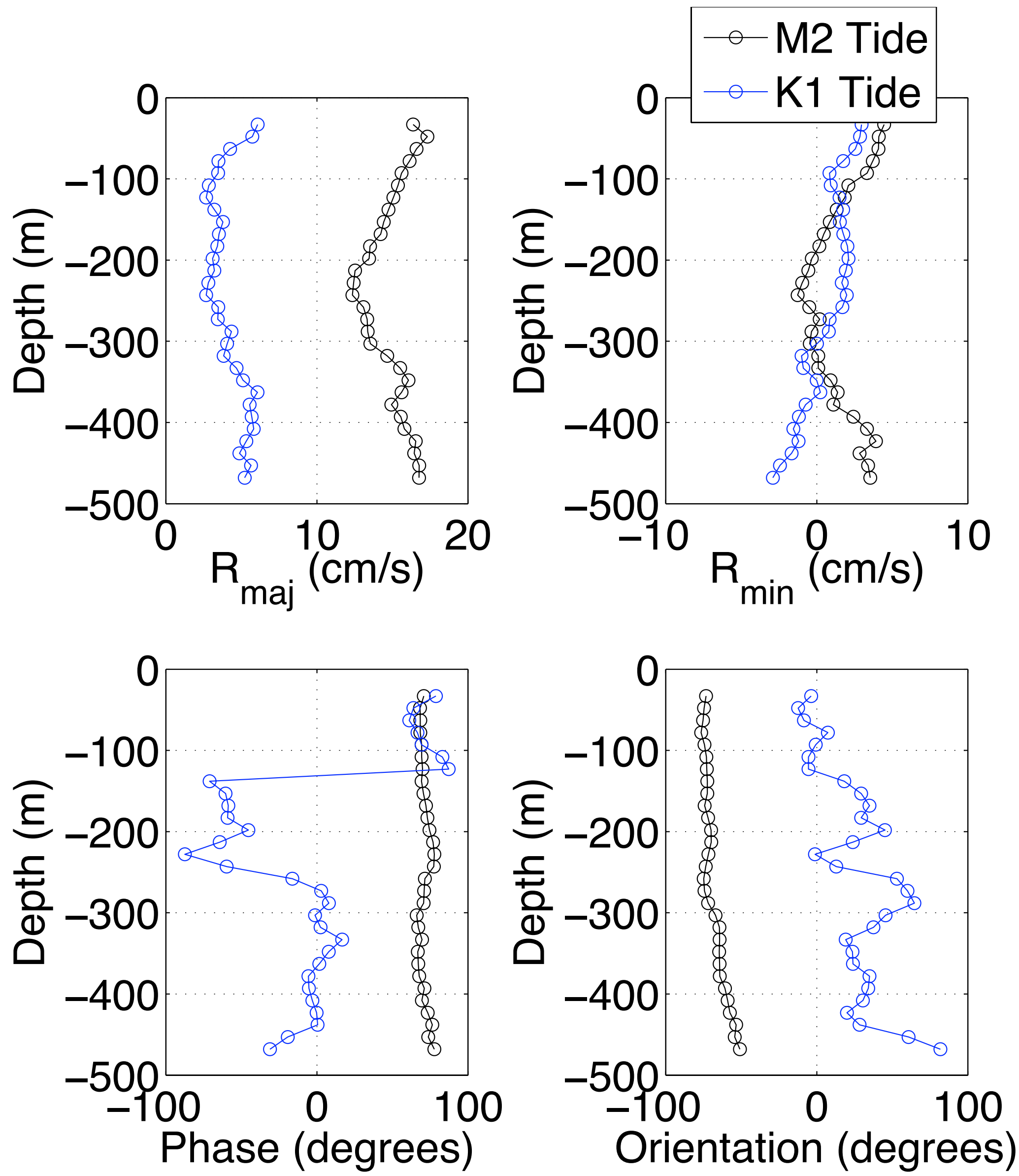

Figure 3.5: Tidal ellipse parameters (semimajor axis [R_{maj}], semiminor axis [R_{min}], orientation, and phase) as a function of depth for the M_2 and K_1 constituents.

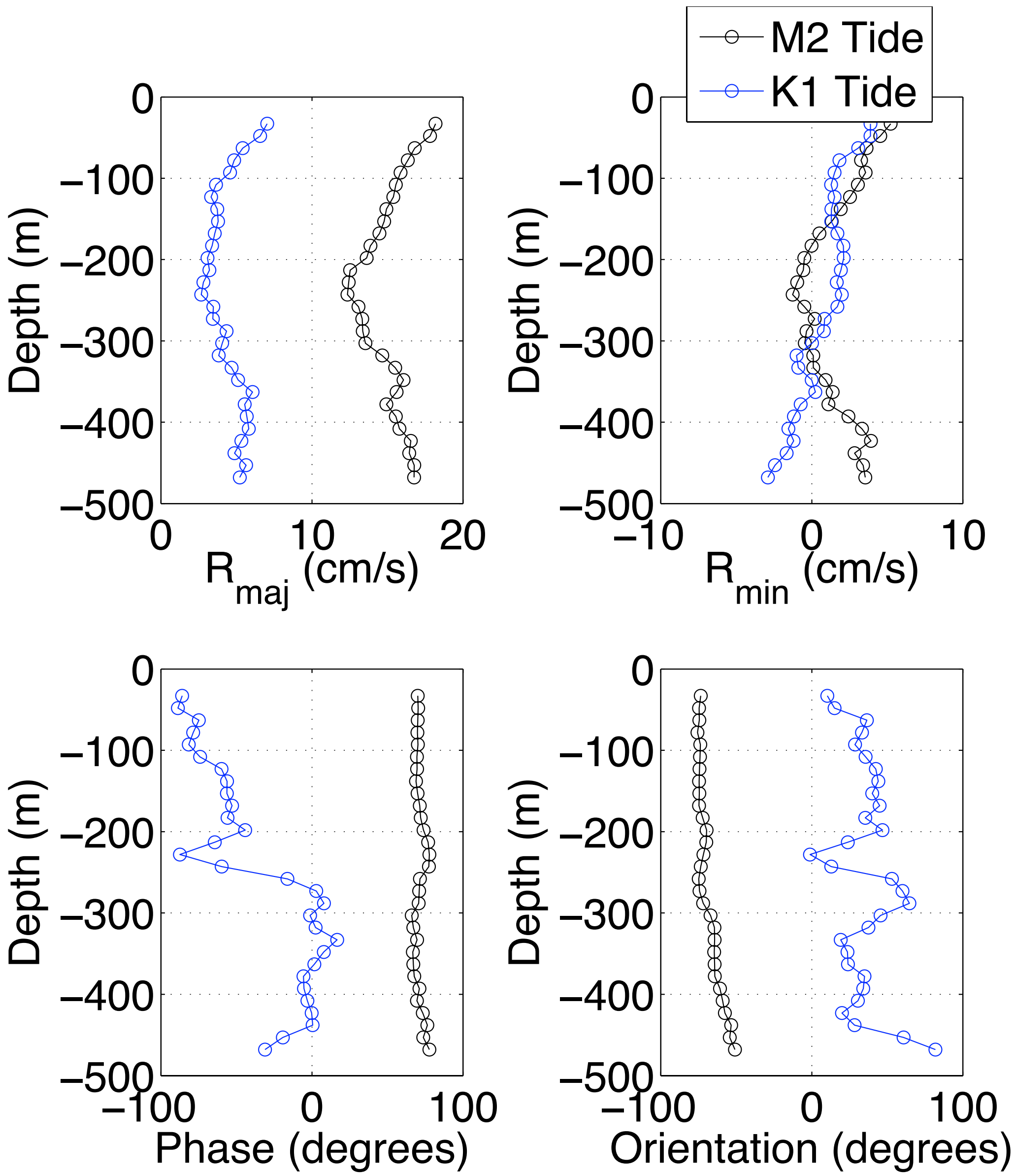

Figure 3.6: Ellipse parameters offshore of the 250 m isobath as a function of depth for the M_2 and K_1 constituents.

specific time may be in the same direction with depth.

Inshore of the 250 m isobath, we find that the M_2 current reaches about 14 cm s^{-1} while the K_1 current reaches approximately 10 cm s^{-1}. There exists some variation in the vertical representation of the K_1 constituent, as seen in Figure 3.7. We find variation in the vertical representation of the orientation and phase. More specifically, the K_1 phase changes by over 100° between 60 and 110 m depth. The orientation also shifts within the same depth range.

From the above analysis, the M_2 constituent is the dominant tidal constituent and shows very little variation in the vertical. The K_1 constituent shows some variation with depth in orientation and phase. The shift occurs at approximately the same depth for both orientation and phase and can be seen in the offshore ellipse parameters as well as the near-shore parameters. However, given the overall consistency in the vertical representation of the constituents, the tidal currents derived from the harmonic analysis are largely barotropic and the tide can be reasonably represented by sinusoidal fitting to depth-averaged data. Examination of vertical and horizontal structure does not result in significant variation of the M_2 tidal parameter.

3.2 Numerical Model

Predictions from the barotropic, numerical tidal model of Padman and Erofeeva (2004) are compared to the tidal signal derived from the harmonic analysis

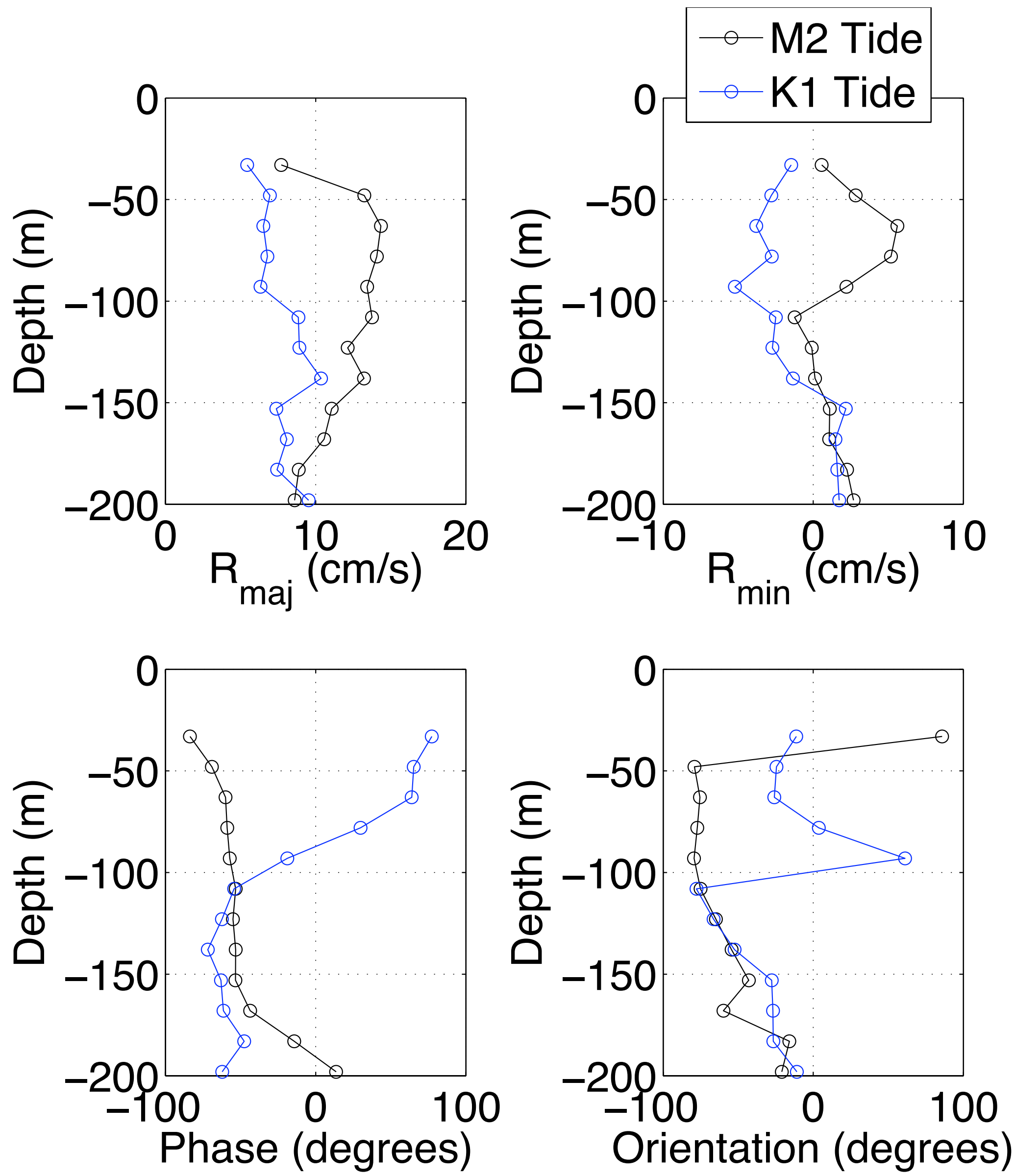

Figure 3.7: Ellipse parameters inshore of the 250 m isobath as a function of depth for the M_2 and K_1 constituents.

discussed above. The tide model domain is organized into seven regions in the high-latitudes of the northern hemisphere based on geography and spatial variations of tidal amplitudes (Padman and Erofeeva, 2004). The predictions are significantly improved over other Arctic tidal models due to higher resolution in areas of complex bathymetry and topography, such as the narrow channels of the Canadian Arctic Archipelago.

The study area is coastal rather than open ocean, hence the geometry of the coastline and the bathymetry are important influences on the tidal response. The model accounts for these factors and employs a 5 km grid in conjunction with the International Bathymetric Chart of the Arctic Ocean (IBCAO; Jakobsson et al., 2000) to predict depth-averaged tidal currents for eight tidal constituents: M_2, S_2, N_2, K_2, K_1, O_1, P_1, and Q_1. The model evaluates the shallow-water equations and, based on those calculations, returns the corresponding tidal signal for specified times and locations.

3.3 Comparison and Results

In Figure 3.8, a comparison of the two distinct tidal signal estimates is made to the depth-averaged ADCP velocity. A dominant along- and across-shore oscillation is clearly discernible and demonstrates tidal significance in the dataset. The predictions from the eight-constituent (four diurnal and four semi-diurnal) barotropic model compare well to the two-constituent (one diurnal and one semi-diurnal) harmonic fit throughout the time series. Only two constituents were used in the harmonic fit due to the short time duration of the data available for this study.

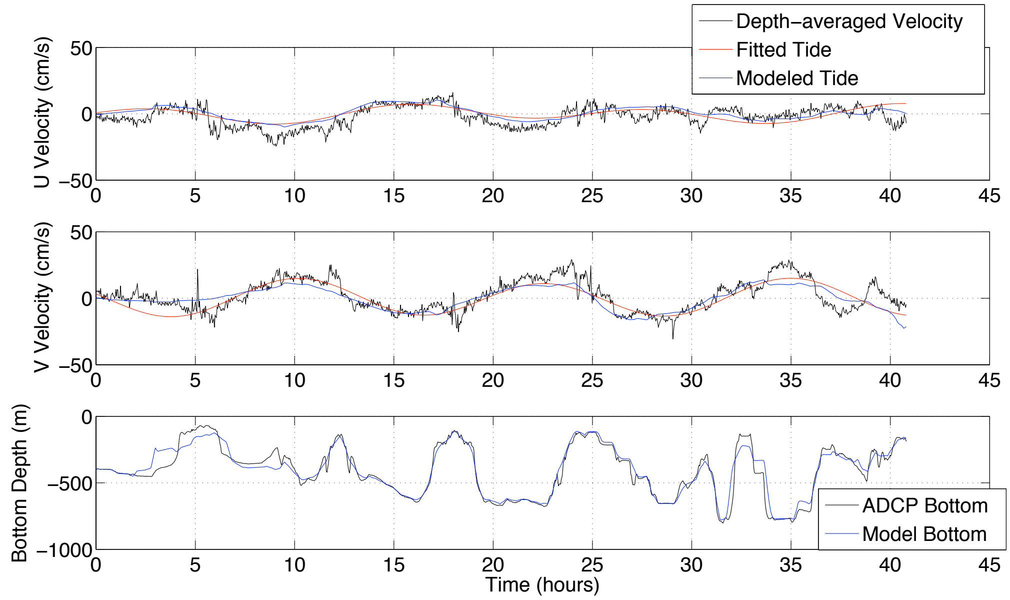

Figure 3.8: In the top two panels, the modeled tide (blue) is compared to fitted tide (red) against the depth-averaged velocity time series (black). The bottom panel shows the similarities between the ADCP tracked bottom (black) and the model bottom depths (blue).

Modeled tidal currents are averaged over the water column and are sensitive to bathymetry. The quality of the model is dependent on the accuracy of the bottom depth. The bottom panel in Figure 3.8 details the differences in the bathymetry from ADCP measurements and from the IBCAO. There is remarkable agreement between the two. The area of greatest disagreement between the modeled and fitted tide generally occurs where there is the greatest discrepancy between the ADCP bottom tracking and the IBCAO. This can be seen in the relatively shallow regions that were surveyed in the first ten hours of the data set.

The similarities between the two tidal estimates validate the harmonic fit, despite the short time interval used. Ellipse parameters for the model tide are obtained by least-squares fitting the time series of the model output. The semimajor axis for the M_2 harmonic fit is approximately 14 cm s^{-1}. The semimajor axis of the model tide is 12.3 cm s^{-1}, consistent with the fitted tide. The semimajor axis for the K_1 harmonic fit is approximately 3.1 cm s^{-1}, while the model tide semimajor axis is 3.3 cm s^{-1}. The model semimajor axis is, therefore, consistent with the values of the semimajor axis of the fitted tide.

In addition to the similarities between the barotropic model results and the harmonic fit, the general lack of vertical variation in the depth-dependent harmonic fit is further evidence that the tides in this region are largely barotropic. The spatially-independent harmonic analysis is used to detide sections A through E and G through J (the sections parallel to the shoreline), but was not used for section F, as it is located a significant distance from the other sections and is governed by different, open ocean dynamics. In this area, poleward flowing currents meet southward flowing currents from Nares Strait. Tides are removed from sections A-E and G-J using the harmonic fit, while section F is de-tided using the barotropic model results.

Chapter 4

HYDROGRAPHY AND GEOSTROPHIC FLOW

4.1 CTD Hydrography

Hydrographic data can be used to determine the relationship between the properties that are observed in the study area and the source waters from which they originate. During the 2003 research cruise, a total of 81 CTD casts were taken. We consider a total of 19 casts that are available in the region of interest for this study: 9 casts along section F, and 5 casts along each of sections A and B. Section F runs south from Cape York into the center of Baffin Bay (see Figure 1.2). Sections A and B are perpendicular to the coastline off of Greenland and extend more than 35 km offshore. The majority of the casts began sampling at 10 m depth, but some have data up to 2 - 3 m from the surface. Salinity, potential temperature, and density were mapped onto a regular grid ($\Delta x \times \Delta z$), where $\Delta x = 2\ km$ and $\Delta z = 25\ m$, using a minimum curvature gridding method (Smith and Wessel, 1990) in Figures 4.2 through 4.4. See Münchow et al. (2006) for a summary of CTD processing techniques.

The potential temperature-salinity ($\theta - S$) diagram in Figure 4.1 illustrates the types of water masses present in this region. Salinity is the main influence on density in the polar regions and, consequently, the lines of constant density are nearly

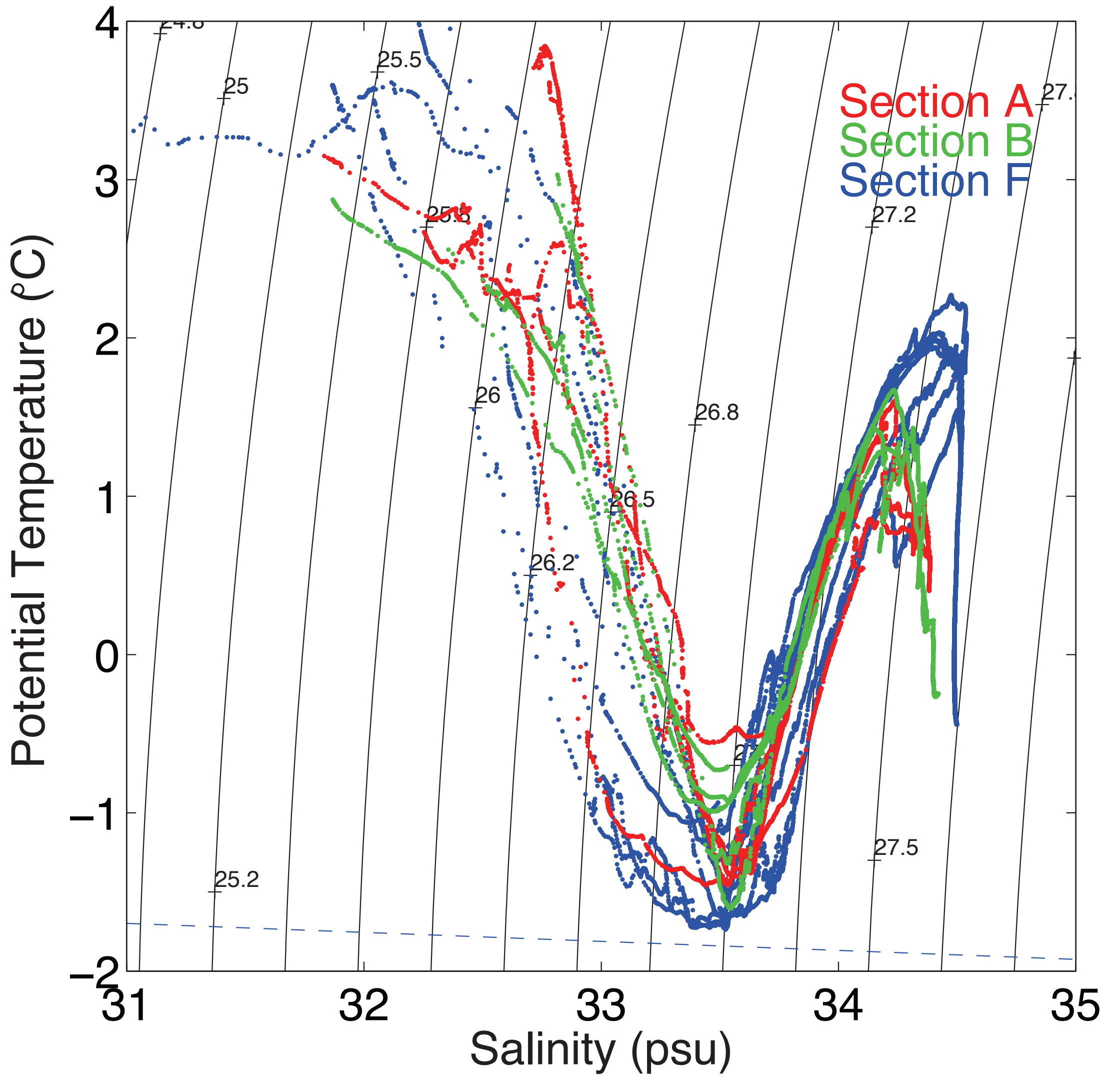

Figure 4.1: Potential temperature (θ) and salinity diagram with density contours (σ_t) for the three hydrographic sections A (red), B (green) and F (blue). Lines of constant density are shown with labels and the dashed line near the bottom indicates the freezing line.

vertical. Because temperature has little effect on density compared to salinity, it can be used as a marker for specific water masses. The subsurface temperature maxima at salinities higher than 34 psu, for example, indicate the presence of Atlantic water in all three sections. The WGC is identified where temperature maxima for each section are greater than 1°C near 34.5 psu. Water entering from Nares Strait to the north is characterized by subsurface temperatures below -0.5°C. In the $\theta - S$ diagram, the temperature minimum near the freezing line at 33.5 psu indicates water that is a remnant of the winter mixed layer.

Figures 4.2, 4.3, and 4.4 illustrate the salinity (psu), potential temperature (°C), and density (kg m^{-3}) for sections A, B, and F. The inverted triangles at the surface indicate the locations of vertical hydrographic data profiles. A structure emerges from the sections with a warm, relatively fresh surface layer to approximately 60 m depth, a thermocline layer centered around 100 m depth with subsurface temperature minima (made up of Pacific influx water), and an ambient bottom layer below approximately 200 m depth that contains subsurface temperature maxima (influenced by the Atlantic). Salinity ranges from approximately 32 psu at the surface to 34.5 psu at the bottom, although there is very low salinity water (28.74 psu) near the coast in section F. Salinity and density decrease near the shore in all sections due to meltwater runoff from Greenland during the summer months and a corresponding wedge of relatively fresh water is visible in each of the sections near the coast. The wedge is thickest near the coast and sloping isopycnals near the surface are indicative of a coastal-trapped, geostrophic surface current discussed in more detail below and in Chapter 5.

In section F, the data reveal a warm (2.27°C), saline (34.5 psu) core centered at approximately 350 m depth over the shelfbreak. Temperatures range from 1.54°C to more than 2°C between 300 m and 600 m depth. These properties are consistent with Atlantic water of the WGC current. This current is also observed in the ADCP velocity data (discussed further in Chapter 5) over the shelfbreak and follows the isobath west across the northern part of Baffin Bay. There is a distinct indication of the WGC $\theta - S$ signature at depth in section B as well. Temperatures range from 1.30°C to 1.67°C between 285 m and 310 m depth. The average salinity in the warm core in section B is 34.25 psu. Section A also reveals the presence of the WGC with temperatures ranging from 1.10 to 1.60°C between 230 m and 310 m depth. The average salinity in the warm core in section A is 34.15 psu. The WGC may also be visible in the velocity data for section A as a sub-surface current at approximately 300 m depth (discussed in Chapter 5).

The hydrographic data indicate that the WGC reaches at least as far north as section A, located at approximately 76.5°N. It is first visible over the shelf in section F as a warm, saline current between 300 m and 600 m depth. While it is argued that most of the current turns cyclonically west across Baffin Bay following the 500 m isobath (Bourke et al., 1989), a branch of the WGC follows the coastline and propagates to 76.5°N. The current maintains an approximate depth of 300 m in sections A and B and loses heat (from more than 2°C to slightly over 1°C) and salinity (34.5 psu to 34.15 psu) as it moves north from section F to section A. This cooling and freshening is most likely due to mixing with the cooler, less saline outflow from the Arctic Ocean and from entrainment of coastal runoff and meltwater.

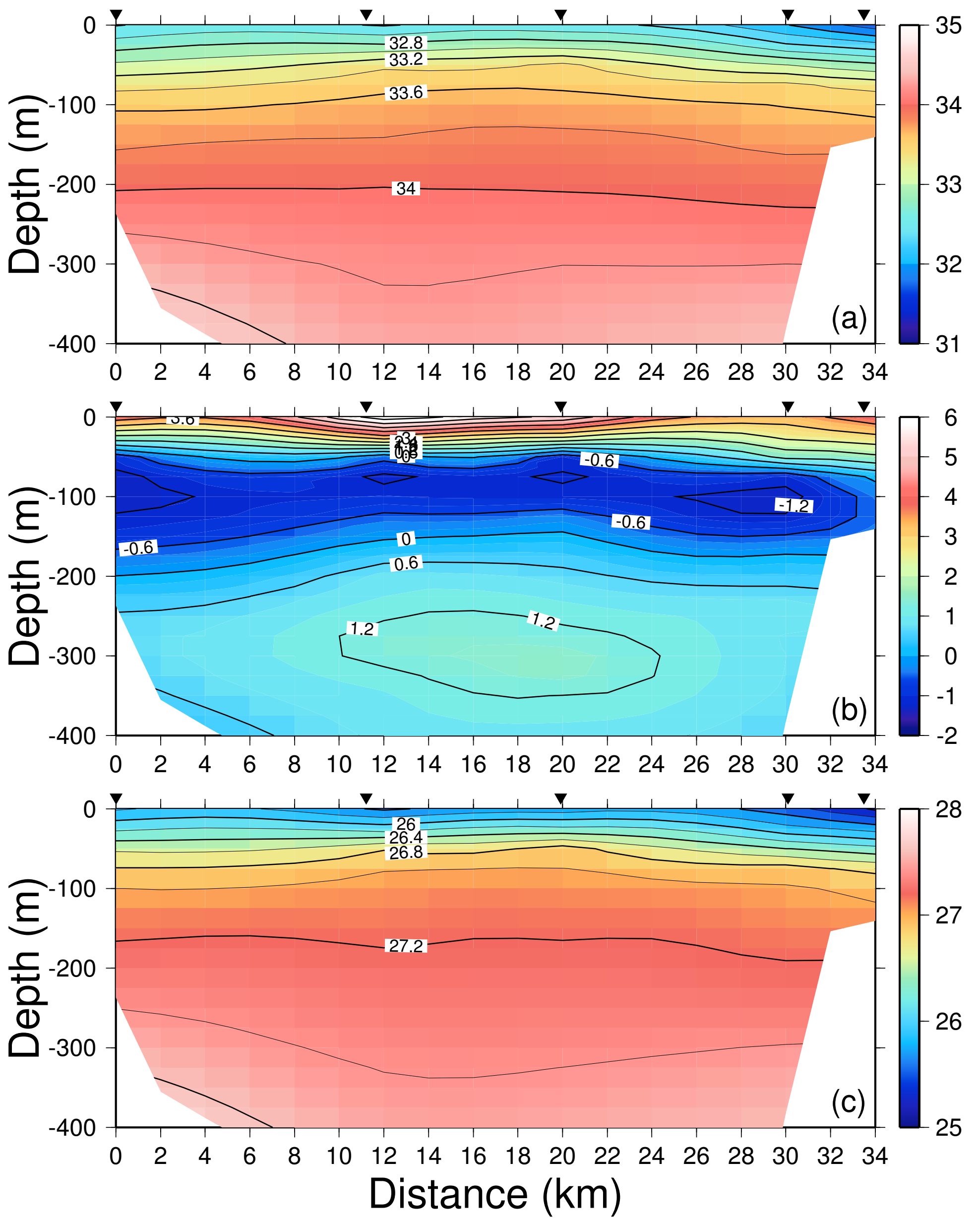

Figure 4.2: Cross section of (a) salinity (psu), (b) temperature (°C) and (c) density (kg m^{-3}) for section A. Inverted triangles indicate the locations of vertical CTD profiles. The coast of Greenland is on the right.

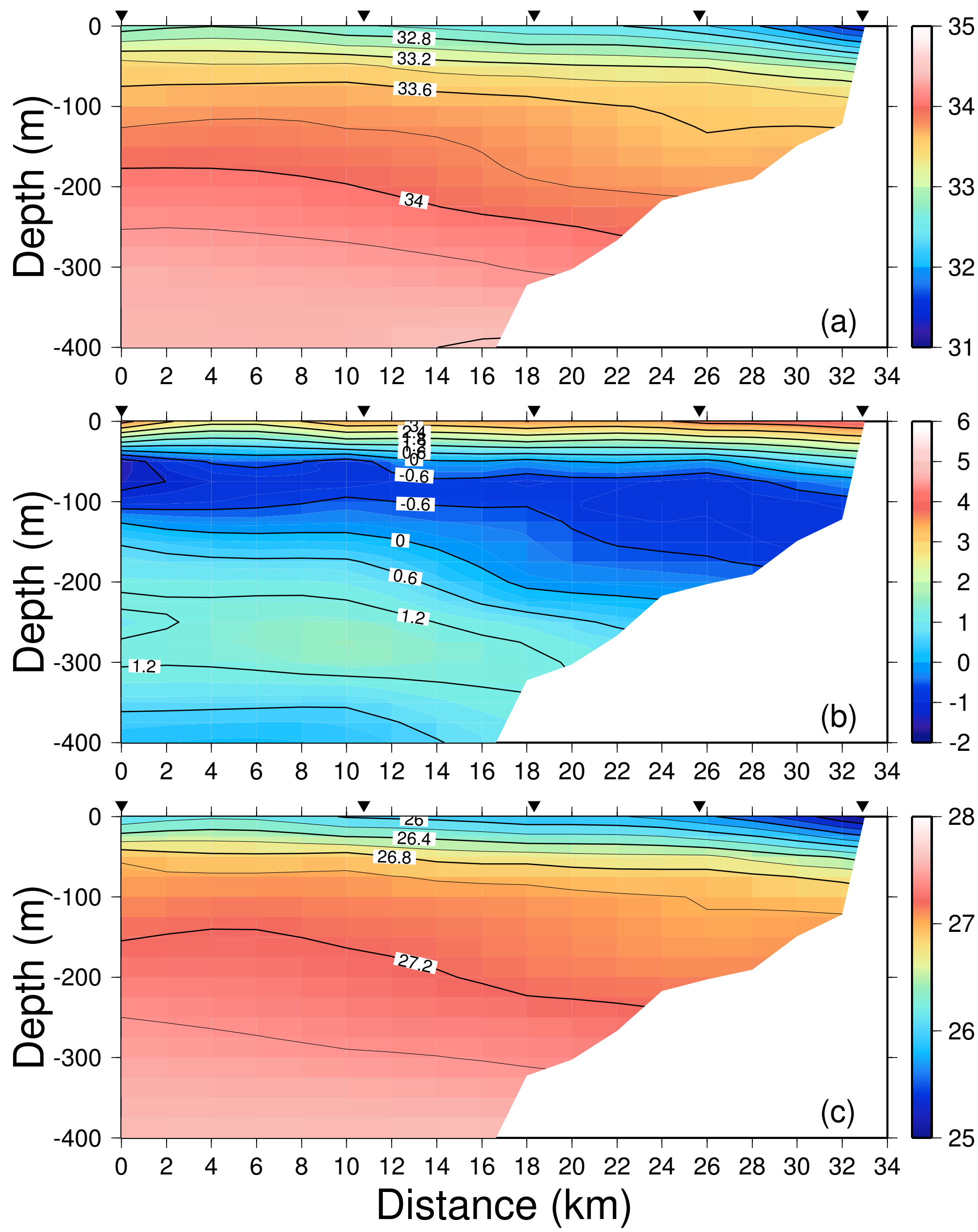

Figure 4.3: Cross section of (a) salinity (psu), (b) temperature (°C) and (c) density (kg m^{-3}) for section B. Inverted triangles indicate the locations of vertical CTD profiles. The coast of Greenland is on the right.

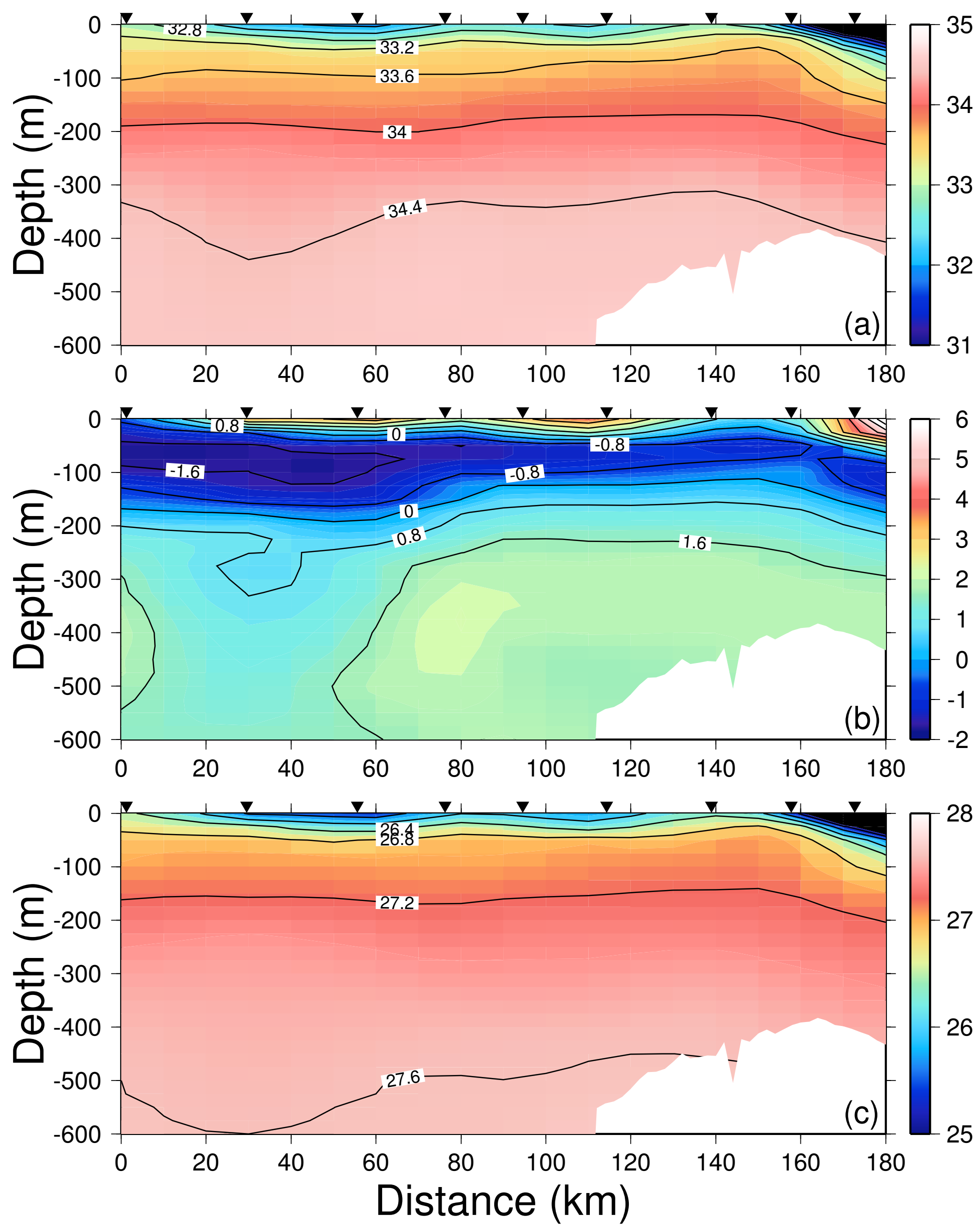

Figure 4.4: Cross section of (a) salinity (psu), (b) temperature (°C) and (c) density (kg m^{-3}) for section F. Inverted triangles indicate the locations of vertical CTD profiles. The coast of Greenland is on the right.

4.2 Geostrophic Dynamics

In geostrophy, the Coriolis force balances the pressure gradient force. In a rotating system, a current can be trapped along a coastline or vertical boundary. An estimate of the horizontal scale of a coastal-trapped current is the Rossby radius of deformation. The Rossby radius is defined as:

$$R = \frac{(\frac{g\Delta\rho D}{\rho})^{1/2}}{f} \sim 7.5 \text{ km} \tag{4.1}$$

where g is the constant of gravity, $\Delta\rho$ is the density difference between two layers of flow, D is the vertical scale of motion, and f is the Coriolis parameter. For this calculation, $g = 9.81$ m s^{-2} and $f = 1.4108 \times 10^{-4}$ s^{-1}, which is the Coriolis parameter for 76°N latitude. To obtain an estimate of the Rossby radius, the values of $\Delta\rho$, ρ and D are derived following the method of Leblond (1980), where the flow is idealized into two layers with distinct densities. Using this method, geostrophic flow is limited to the upper layer (ρ_1) and the lower layer (ρ_2) remains at rest (Leblond, 1980). In this case, hydrography data is used to find $\rho_1 = 1026$ kg m^{-3} (which becomes ρ) and $\rho_2 = 1027.2$ kg m^{-3}. The value of $\Delta\rho$ is then 1.2 kg m^{-3} and the value of D (the thickness of the upper layer at the boundary) is 100 m. Using these values, we calculate a Rossby radius of 7.5 km, which is consistent with the scale of flow observed in the velocity field (discussed in the next Chapter) and in the geostrophic currents (Figures 4.5 through 4.7). It is important to resolve the Rossby radius so that the baroclinic nature of the flow field can be accurately estimated. Our ADCP velocity data accurately resolve the internal Rossby radius; however, the hydrography data is not as high resolution. CTD section spacing is on the order of the Rossby radius.

Thermal Wind Balance

When freshwater enters the ocean through runoff or melt, changes in the density structure and subsequent horizontal pressure gradients drive geostrophic currents. It is this type of current that is expected due to freshwater influx from the coast of Greenland during the summer months. This increase of freshwater induces a cross-shelf pressure gradient with higher pressure near the coast than further offshore and drives the current in the direction of Kelvin wave propagation, which is observed in the velocity data (Garvine, 1999; see Chapter 5).

The thermal wind balance, derived from the geostrophic momentum balance, is:

$$\frac{\partial v_g}{\partial z} = -\frac{g}{f\rho_0}\frac{\partial \rho}{\partial x} \tag{4.2}$$

where $\frac{\partial v_g}{\partial z}$ is the along-shelf geostrophic velocity shear, ρ_0 is a constant reference density, g is the constant of gravity, f is the Coriolis parameter, and $\frac{\partial \rho}{\partial x}$ is the across-shelf horizontal density gradient (Gill, 1982). For stratified flows and baroclinic processes, the thermal wind equation is used to examine the velocity shear between layers. For the purposes of this study, we take advantage of the available ADCP data and use measured velocities at a selected reference depth. The observed density field from CTD data is then used to determine vertical velocity shear through the sections (i.e., the baroclinic component of the flow that corresponds to horizontal density variations).

For this calculation, ADCP measured velocities are used at reference depth $z_0 = 93$ m and then integrated upward to the surface and downward to the bottom to obtain the along-shore geostrophic velocities (normal to the section). At a depth of 93 m, ADCP data is available at every distance across each of sections A, B, and F. Thus,

$$v_g(x,z) = v_0(x,z_0) + \int_{z_0}^{z} \frac{-g}{\rho_0 f} \frac{\partial \rho}{\partial x} dz \tag{4.3}$$

where v_0 is the reference velocity from ADCP measurements at reference depth z_0 and reference density, ρ_0, is 1028 kg m^{-3}. By employing this method, comparisons can be made between geostrophic currents derived from the density fields and measured ADCP velocities (discussed in Chapter 5).

Figures 4.5, 4.6, and 4.7 illustrate the geostrophic velocity sections A, B, and F. Positive velocities are in the direction of Kelvin wave propagation (poleward). Notable features include the surface-intensified current (velocities greater than 20 cm s^{-1}) in all three sections and the subsurface jet in section A (velocity greater than 10 cm s^{-1}, which is also visible in the ADCP data; see next Chapter). Section F exhibits a subsurface current over the shelfbreak as well as a possible anti-cyclonic eddy described in detail by Münchow et al. (2011) (also visible in the ADCP measured velocities in Chapter 5).

Estimates of the volume flux from the geostrophic sections can be found in Table 1. This table shows that the estimates of volume fluxes from hydrography are on the order of the volume fluxes calculated from ADCP velocity data.

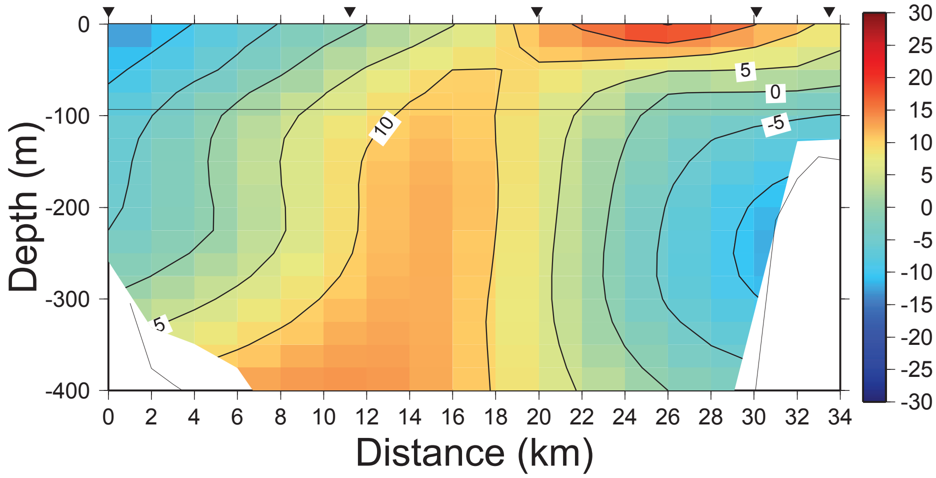

Figure 4.5: Geostrophic velocity (cm s^{-1}) for section A. Red shading indicates poleward flow, while blue shading indicates equatorward flow. Inverted triangles indicate the locations of vertical CTD profiles. The horizontal line represents the location of ADCP reference velocities.

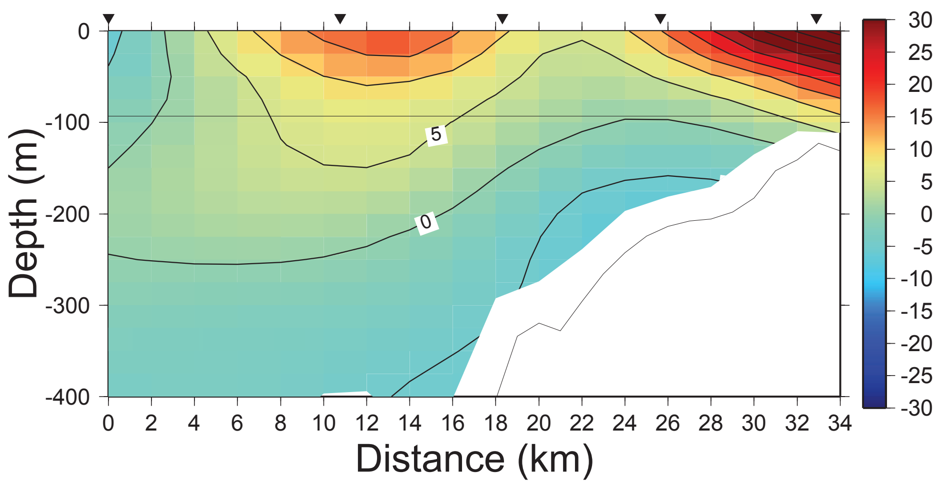

Figure 4.6: Geostrophic velocity (cm s^{-1}) for section B. Red shading indicates poleward flow, while blue shading indicates equatorward flow. Inverted triangles indicate the locations of vertical CTD profiles. The horizontal line represents the location of ADCP reference velocities.

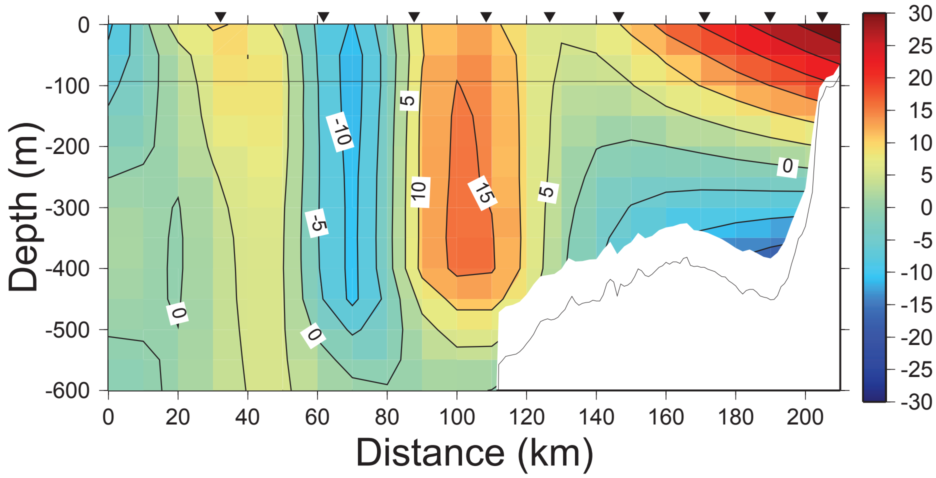

Figure 4.7: Geostrophic velocity (cm s^{-1}) for section F. Red shading indicates poleward flow, while blue shading indicates equatorward flow. Inverted triangles indicate the locations of vertical CTD profiles. The horizontal line represents the location of ADCP reference velocities.

Chapter 5

SUB-TIDAL VELOCITY

5.1 ADCP Velocity

ADCP along-shore velocities for sections A through F (see Figures 5.1 - 5.6) were generated using sub-tidal currents derived from the removal of tidal signals as discussed in Chapter 3. After extrapolation to the surface by linear regression using data from 33 m to 78 m below the surface, the velocities in each of the sections were interpolated onto a regular grid ($\Delta x \times \Delta z$), where $\Delta x = 2$ km and $\Delta z = 25$ m using continuous curvature gridding algorithm *surface* (see Smith and Wessel, 1990). Data in the bottom 15% of the water column were omitted due to ADCP interference.

Figures 5.1 through 5.6 illustrate the along-shore, sub-tidal velocities as cross-sections in the (x, z) plane. Red contours (positive velocities) indicate poleward flow, while blue contours (negative velocities) indicate equator-ward flow. The most pronounced feature visible in the figures is an along-shore surface current (greater than 30 cm s^{-1}) that exists in all sections, although it varies slightly in width. With the exception of a sub-surface current at a depth of about 300 m in section A and subsurface flow in section F, the other sections B - E exhibit little flow below approximately 100 m depth. There is evidence of weak return flow at depth in each of the sections that can also be seen in the thermal wind sections in Chapter 4.

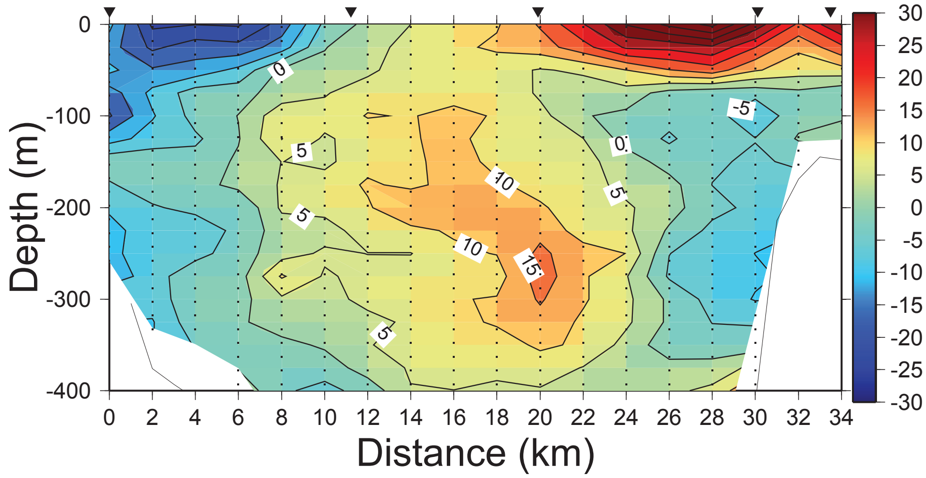

Figure 5.1: Section A along-shore velocity (cm s^{-1}). Small points indicate ADCP data locations and the inverted triangles indicate CTD station locations. Greenland is on the right.

In general, the sections exhibit very little cross-shore flow with average cross-shore velocities less than 0.1 cm s^{-1}.

In each section, the maximum surface velocity is greater than 30 cm s^{-1}. The surface current largely follows the bathymetry along the coast and remains within 100 m of the surface. The width of the current varies slightly as it propagates poleward along the coast from section E to section A. The current is likely driven primarily by a wedge of freshwater adjacent to the coast that was observed in the hydrographic data (discussed in Chapter 4), due to meltwater runoff from Greenland that induces lateral pressure gradients.

In addition, there is a subsurface current in section F with velocities greater than 15 cm s^{-1} over the shelfbreak at km-110. Corresponding $\theta - S$ measurements suggest that this is part of the WGC. Münchow et al. (2011) refer to this as the

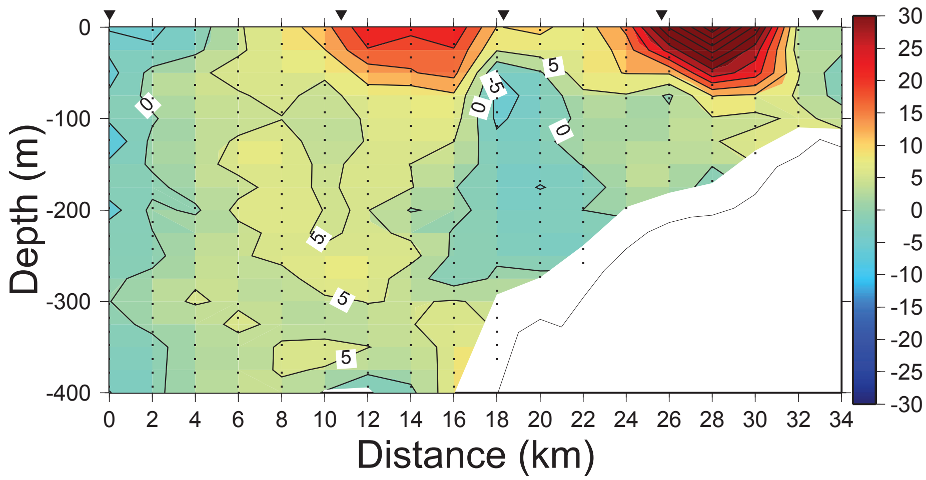

Figure 5.2: Section B along-shore velocity (cm s^{-1}). Small points indicate ADCP data locations and the inverted triangles indicate CTD station locations. Greenland is on the right.

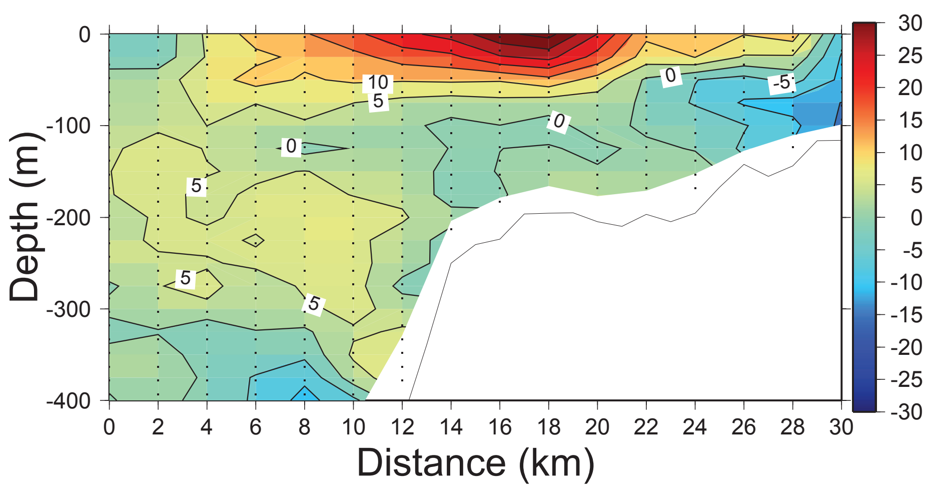

Figure 5.3: Section C along-shore velocity (cm s^{-1}). Small points indicate ADCP data locations. Greenland is on the right.

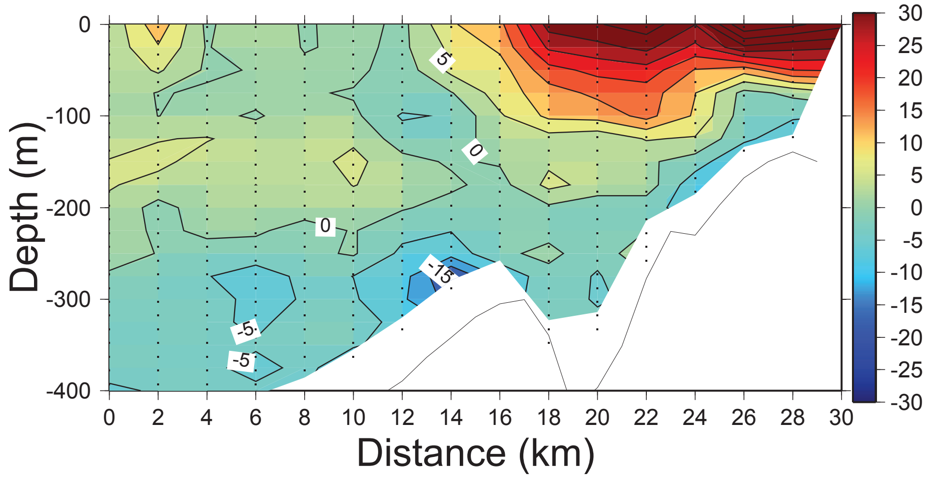

Figure 5.4: Section D along-shore velocity (cm s^{-1}). Small points indicate ADCP data locations. Greenland is on the right.

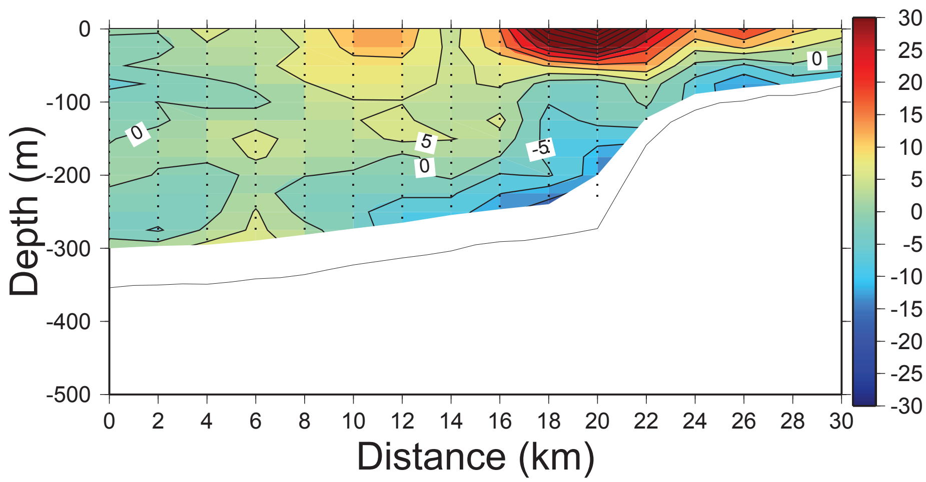

Figure 5.5: Section E along-shore velocity (cm s^{-1}). Small points indicate ADCP data locations. Greenland is on the right.

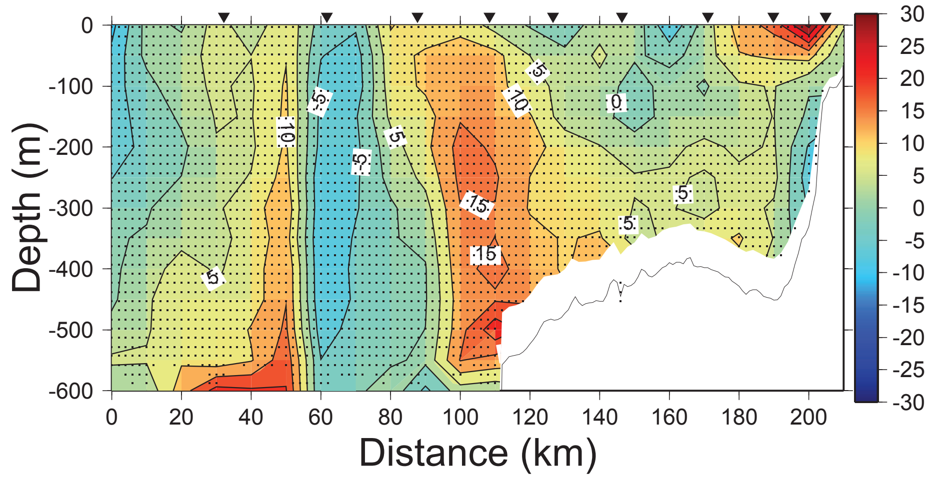

Figure 5.6: Section F along-shore velocity (cm s^{-1}). Small points indicate ADCP data locations and the inverted triangles indicate CTD station locations. Greenland is on the right.

West Greenland Slope Current. There is also a sub-surface current near the center of section A at approximately 300 m depth that is not present in the other sections. This is the part of the WGC identified in the hydrographic data. Sections B through E are not situated far enough offshore to resolve the subsurface flow. Temperature and salinity signatures in the hydrographic data of both sections A and B suggest, however, that the WGC reaches these latitudes.

As noted in the section on geostrophic velocity, an anti-cyclonic eddy feature is present at km-50 in section F. Münchow et al. (2011) discuss this feature in detail and show that it can be modeled as a Rankine vortex (Münchow et al., 2011).

De-tided, depth averaged velocity vectors are presented in Figure 5.7. This figure reveals a general along-shelf flow pattern in all sections. Notably, there is a

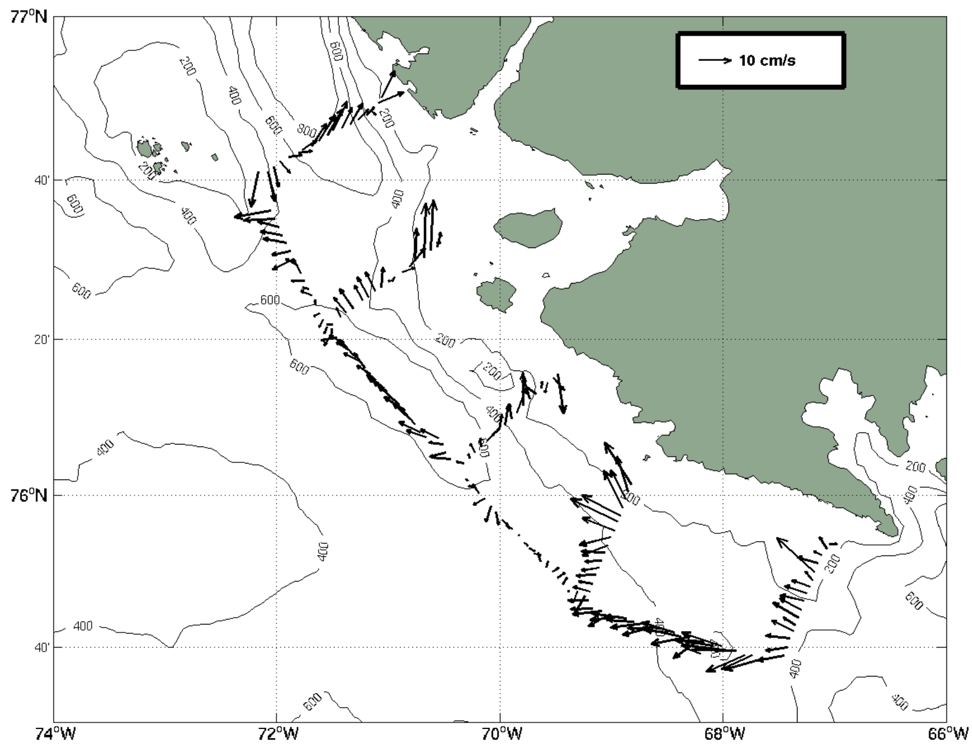

Figure 5.7: Depth-averaged, detided ADCP velocity vectors.

southward current visible in section A that suggests possible anti-cyclonic (clockwise) circulation around the Carey Islands (also visible in cross-section A in Figure 5.1 above). Depth averaged vectors over the top 100 m only are presented in Figure 5.8 and indicate that the flow is intensified near the surface.

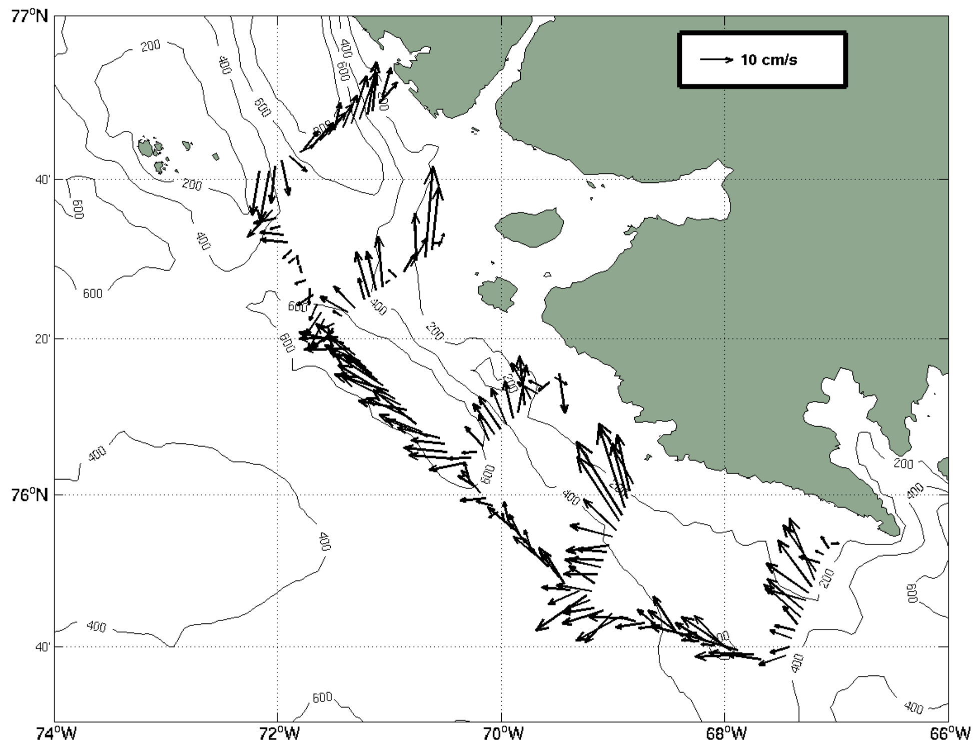

Figure 5.8: Detided ADCP velocity vectors averaged over the top 100 m of the water column.

5.2 Volume Flux

Volume flux is defined as:

$$q = \int v(x, z)dxdz \tag{5.1}$$

where $v(x, z)$ is the velocity normal to the area in the (x, z) plane.

Total volume and freshwater fluxes are summarized in Table 5.1. Estimates of flux are made, but do not account for the bottom 15% of the water column (due to ADCP interference and filtering discussed in Chapter 2). However, the estimates do include the top 30 m of the water column where data have been extrapolated using linear regression (ADCP data is unavailable within 30 m of the surface due to ship draft and a blanking interval for transducer ring down). The extrapolation method used only provides an estimate of surface currents. This is a serious concern as the strongest currents and freshest waters are located in the top 30 m of the water column and are crucial in the determination of volume and freshwater flux.

The sectional area increases from section E to section A, and we find that the magnitude of volume flux increases correspondingly. All estimates through sections A to E are positive, indicating net poleward fluxes. Section A has a total volume flux of 0.51 Sv. Approximately 60% of the total flux is due to subsurface currents located between km-10 and km-20 and 100 m and 400 m depth as seen in Figure 5.1. The other 40% can be explained by the near surface current close to the coastline.

Table 5.1: Volume fluxes (Sv) for across-shelf (A through F) and along-shelf (G through J) sections (including measured ADCP velocity sections and calculated geostrophic velocity sections). Freshwater fluxes (mSv) are included for sections A, B, and F.

Section	**Total Volume Flux**	**Volume Flux top 100 m**	**Freshwater Flux**	**Freshwater Flux top 100 m**	**Freshwater Flux top 30 m**	**Geostrophic Volume Flux**
A	0.51	0.19	17	11	8	0.51
B	0.49	0.30	20	16	11	0.24
C	0.26	0.18	—	—	—	—
D	0.24	0.29	—	—	—	—
E	0.16	0.15	—	—	—	—
F	4.79	—	97	—	—	4.13
G	0.02	—	—	—	—	—
H	0.65	—	—	—	—	—
I	-0.12	—	—	—	—	—
J	-0.09	—	—	—	—	—

The method used here to calculate volume flux will only provide a rough estimate due to the fact that the lowest 15% of the water column is not included in the calculations and the surface velocities are extrapolated. In addition, the sections do not actually reach the physical coastline. There are approximately 5-10 km between the ends of the sections that run perpendicular to the coast and the actual coastline, and because the width of a current in geostrophic balance scales with the internal Rossby radius of deformation (Gill, 1982), fluid flow within this distance may contribute a large amount to the actual flux of water through the sections.

5.3 Freshwater Flux

Freshwater flux is defined as:

$$F = \int v(x,z)(1 - \frac{S(x,z) + s_t}{S_0})dxdz \tag{5.2}$$

where $S(x,z) + s_t$ is the measured salinity including the unknown tidal component of the salinity field and $v(x,z)$ is the velocity normal to the area (x,z) (Münchow et al., 2006). The salinity fields used in this calculation can been seen in Figures 4.2, 4.3, and 4.4 in Chapter 4. The velocity fields for sections A, B, and F can be seen in Figures 5.1, 5.2 and 5.6, respectively. Freshwater fluxes for sections C, D, and E are not calculated due to lack of hydrographic (i.e., salinity) data available. The removal of the tidal signal using harmonic analysis was discussed in Chapter 3, but we note that the salinity data may still contain unknown tidal fluctuations. Reference salinity S_0 is chosen to be 34.8 psu to facilitate comparisons between the estimates made here and those commonly used in the literature (Melling, 2000; Münchow et al., 2006; Dickson et al., 2007).

Most of the freshwater flux occurs in the upper 100 m of the water column where the fastest currents and lowest salinities can be found. This is expected due to meltwater and glacial runoff. Therefore, an accurate estimate of freshwater flux is highly dependent on the values of salinity and velocity in the portions of the water column where ADCP data does not exist. The flux through the top 30 m of the water column is especially important in calculations of freshwater flux as indicated by Table 5.1. 63% of the freshwater flux is located in the top 100 m of the water column in section A and 82% in section B, and in fact, most of this flux is located within the top 30 m. This is an important source of uncertainty in the calculations presented here.

There is a poleward freshwater flux of 17 mSv (10^3 m^3 s^{-1}) through section A and 20 mSv for section B. Section F, which extends approximately 220 km south into Baffin Bay, has a freshwater flux of 97 mSv. Freshwater is most likely delivered to the system as runoff from melting Greenland ice. Other sources of freshwater input could include melting sea ice and precipitation, though sea ice was not observed in this area during the summer months (see Figure 2.1).

Chapter 6

OTHER FORCES

6.1 Wind Fields

Figure 6.1 depicts wind velocity vectors that were collected on board the USCGC *Healy* during the research expedition in 2003. Data were collected every five minutes. Sections A, B, and C are characterized by predominantly alongshore winds in a south-east direction, while section D has westward winds and E has predominantly northward winds. This reversal in wind direction can be clearly seen in Figures 6.1 and 6.2, which show a map of the wind vectors and a time series of the wind data, respectively. In addition to the topography of the adjacent landscape, wind in this region is also influenced by pressure differences between the Arctic Ocean and northern Baffin Bay (Samelson et al., 2006). Samelson et al. (2006) show that wind along Nares Strait is well correlated with the sea level pressure difference along the Strait. Features such as the opening of the North Water polynya and the amount of sea ice present in Nares Strait are also connected to the wind stress in this region.

Figure 6.2 shows a time series of the collected wind data and also a time series of the de-tided ADCP velocity data at a depth of 33 m below the surface (the depth of the most near-surface velocity measurement). As noted above, a shift

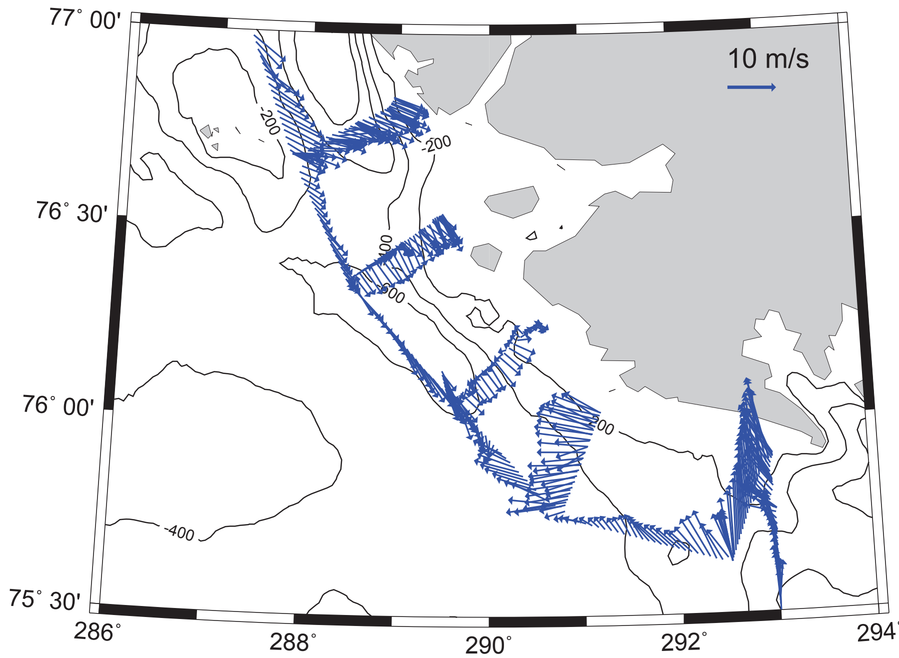

Figure 6.1: Wind velocity vectors as measured every five minutes along the *Healy* ship track.

in the winds around hour 15 from a relatively strong along-shore regime can be seen in the Figure. The mean magnitude of the wind over the entire time series is 7.2 m s^{-1} and peak winds are observed at approximately hour 7 with a magnitude of 17.4 m s^{-1}.

To examine any potential relationship between ADCP measured velocities and the wind field, we calculate the correlation coefficient between the two time series. We find no correlation between the wind stress and the ADCP velocities at any measured depth. Similarly, there is no correlation between wind stress and the depth-averaged ADCP velocities. This result indicates that the flow in this region is primarily influenced by forces other than wind stress, namely, density gradients and stratification (baroclinicity), and rotation (Coriolis). However, data collected at time scales longer than the present data set may reveal a stronger relationship between the wind stress and velocity measurements.

6.2 Internal Friction

To examine the internal structure of the flow, complex correlation methods were applied to each successive layer of ADCP measured velocity (measured at 15 m depth intervals for all sections) with the topmost layer at 33 m depth. This allows for an examination of the potential relationship between the top layer of flow with each successive layer in the water column. The picture that emerges from this analysis provides information on the nature and structure of the flow in this region.

First, the tidal signal and mean were removed from the data. The complex

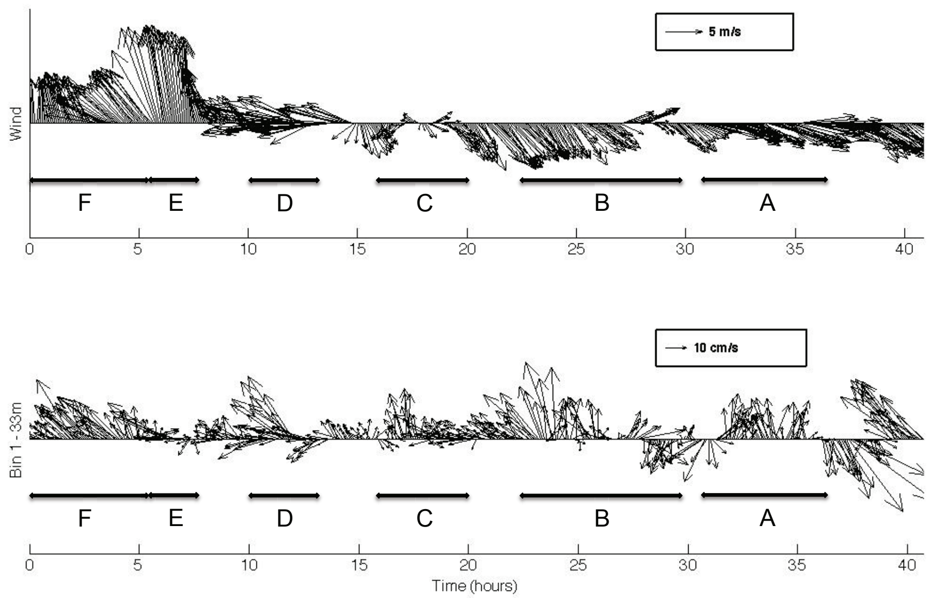

Figure 6.2: Time series of wind data (top) and current velocity (bottom) at 33 m depth (the depth of the most near-surface ADCP measurements). The times for each of the across-shelf sections are indicated with arrows.

horizontal velocity vector is then represented by $w(t) = u(t) + iv(t)$, where $i = \sqrt{-1}$. Following the method of Kundu (1976), the complex correlation coefficient can be written as:

$$r = c \sum_{i=1}^{N} w_{i1}(t_i) \cdot w_{i2}(t_i) \tag{6.1}$$

where $c = 1/[N < w_1{}^* w_1 >^{\frac{1}{2}} < w_2{}^* w_2 >^{\frac{1}{2}}]$ and the asterisk indicates the complex conjugate. The complex correlation coefficient can then be written as:

$$r = \frac{< u_1 u_2 + v_1 v_2 > + i < u_1 v_2 - u_2 v_1 >}{< u_1{}^2 + v_1{}^2 >^{\frac{1}{2}} < u_2{}^2 + v_2{}^2 >^{\frac{1}{2}}} \tag{6.2}$$

and is shown in Figure 6.3 for each depth level. As one might expect, the values of the magnitude of the correlation decrease with increasing depth. This indicates that the near-surface layers are more closely related to the 33 m depth layer than the near-bottom layers.

According to Kundu (1976), the corresponding phase angle, α (which indicates the average angular displacement of the velocities with respect to the surface layer) can be written as:

$$\alpha = \tan^{-1} \frac{< u_1 v_2 - v_1 u_2 >}{< u_1 u_2 + v_1 v_2 >} \tag{6.3}$$

and can be seen in Figure 6.4. The positive angles shown here indicate that the angle of the velocity in each layer is rotated to the right of the velocity in the surface (33 m) layer. The angle increases with increasing depth and shows veering of the velocities with depth.

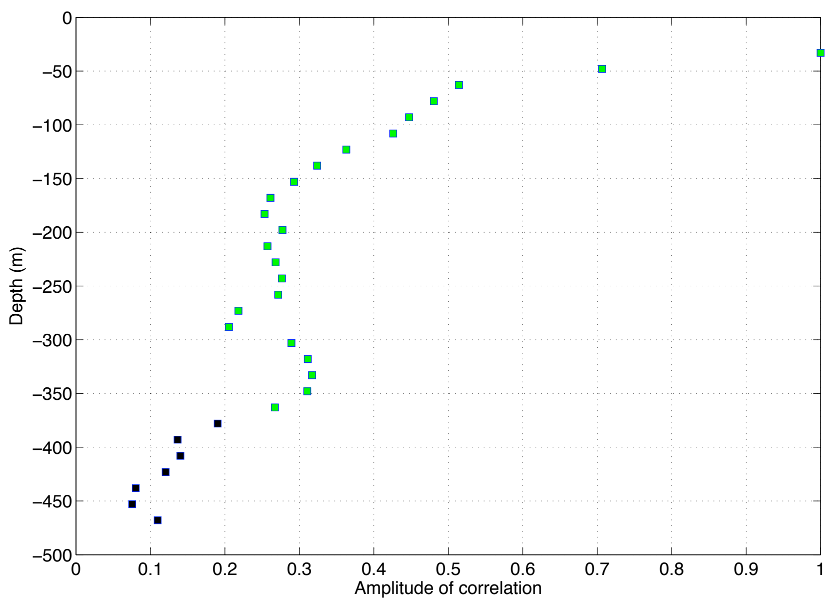

Figure 6.3: Correlation coefficients (r) for each depth level with respect to the surface layer at 33 m depth. Statistically significant values at the 95% level are shown in green.

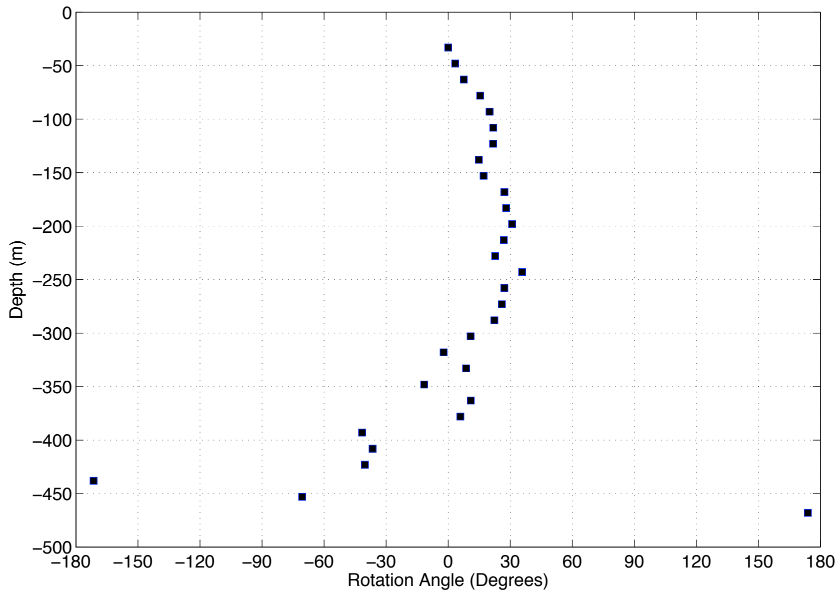

Figure 6.4: Rotation angle (in degrees) of each layer in the water column with respect to the surface layer at 33 m depth.

Statistical Significance

To test the significance of the correlations shown above, the method of Sokal and Rohlf (1981) is used. We use this method to find the 95% significance levels for the correlation coefficients. First, to calculate the number of independent degrees of freedom, the auto-decorrelation times are used to find an approximation of the lag time in this data set. This is found to be approximately 0.4 hours. Using this information, the number of degrees of freedom (n) is calculated by dividing the total number of hours in the data set by 0.4 hours.

Next, the null hypothesis is tested with the Students t-test using the following:

$$t_s = r\sqrt{\frac{(n-2)}{(1-r^2)}} \tag{6.4}$$

where r is the correlation coefficient and n is the number of degrees of freedom. If the probability of t_s is less than 0.05, we reject the null hypothesis and acknowledge that the correlation coefficient is statistically significant at the 95% confidence level (see Figure 6.3) (Sokal and Rohlf, 1981). Correlation coefficients are shown to be statistically significant to a depth of approximately 370 m.

Chapter 7

SUMMARY AND CONCLUSIONS

Volume and freshwater fluxes play a major role in the ocean circulation of the polar regions. ADCP, CTD, and wind data were collected on the USCGC *Healy* during the summer of 2003, and this data set (located near Thule, Greenland) gives a snapshot view of the structure and circulation of currents in this region. Previous work by Melling et al. (2001) and Bacon et al. (2002) provides some context for the dynamics at work in this region. In particular, a surface, buoyancy-driven current is examined as well as the presence of the West Greenland Current.

As a preliminary analysis of the tidal currents, a comparison is made between the depth averaged velocity data and a harmonic fit using one diurnal and one semidiurnal tidal constituent. We further refine the analysis and allow tides to vary both horizontally and vertically. Ellipse parameters as a function of depth are calculated and reveal that the tides are primarily barotropic. To further validate this result, a comparison is made between the predictive barotropic tide model of Padman and Erofeeva (2004) and the harmonic fit of data from the study area, which reveals excellent agreement between the two.

De-tided ADCP velocities reveal a persistent surface-intensified current in the direction of Kelvin wave propagation that corresponds to a freshwater wedge in the hydrography data. The current reaches maximum speeds greater than 30 cm s^{-1}. While it varies somewhat in width, the current exists above 100 m depth in each of the sections. The width of the surface current compares well to the internal Rossby radius of deformation ($\sim$ 7.5 km). This suggests that the subtidal flow is influenced both by vertical and horizontal density stratification (baroclinicity) as well as rotation (Coriolis). We note that it is important to resolve the Rossby radius correctly by sampling to describe physical flow features without aliasing.

CTD hydrography data indicate that a poleward branch of the WGC propagates towards southern Smith Sound and is present as far north as 76.5°. Hydrography data reveal a three-layer geostrophic density structure including a warm surface layer, a thermocline layer centered at approximately 100 m, and an ambient layer below 200 m depth. The freshest water is located at the surface and next to the coast in all of the sections and is visible as a low-salinity wedge in Figures 4.2, 4.3, and 4.4.

In geostrophy, the Coriolis force balances the pressure gradient force and currents flow parallel to the isobars, with higher pressure on the right in the Northern Hemisphere. The thermal wind balance provides a purely geostrophic velocity field from the hydrography data. We use ADCP velocity as a reference at a depth of 93 m. This exercise provides a comparison with the ADCP velocity cross-sections and the volume fluxes are calculated for both the measured ADCP and geostrophic sections. The fluxes are found to be on the same order of magnitude, indicating the strong influence of geostrophy on the currents in this region.

Volume flux through the sections is positive, indicating poleward, along-shelf flow. There is uncertainty in the flux estimates related to the missing data in the space between the end of each section and the physical coastline, since this distance is on the order of the Rossby radius of deformation. The bottom 15% of the water column is not included in these calculations, and this could result in an underestimation of the true velocity flux. There is also uncertainty within the top 30 m of the water column due to extrapolation of data to the surface where ADCP data does not exist. To improve the estimates of volume and freshwater fluxes, future efforts could include data collected closer to the physical coastline as well as improved methods to estimate velocities within the top 30 m of the water column, where possible. In addition, cross-shore sections should extend further offshore to capture the sub-surface signature of the WGC in all sections.

Freshwater flux is calculated for sections A, B, and F. To obtain these values, it is necessary to extrapolate the velocity and salinity fields to the surface, as most of the freshwater is located in the top 100 m of the water column. The total volume and freshwater fluxes for all of the available sections have been summarized in Table 5.1.

A preliminary examination of the wind data collected on board the *Healy* reveals no correlation between the wind stress and the velocity vector field. Comparisons were made between the wind time series and the surface velocity vectors as well as the depth-averaged velocities. Internal structure is evaluated by a complex correlation analysis of velocity vectors at each successive depth layer in the water column with respect to the most near-surface layer where data is available (33 m). Correlation coefficients and phase angles are calculated and are found to be statistically significant to approximately 370 m. The positive phase angles indicate velocity veering (to the right of the surface layer) with depth.

There are a number of considerations that emerge from this work that can be applied to future study in this region. Further consideration of data at longer time scales would enable the calculation of seasonal variations in the surface current and the WGC. Some important questions include: How have recent increases in sea ice melt in the Arctic, and glacial and ice sheet melt on Greenland influenced the currents in this region? How do changes in weather and precipitation affect coastal circulation? What are the seasonal changes in heat and freshwater flux through the region and how does this influence circulation and productivity in Smith Sound? These are questions that can be answered by integrating numerous types of data sets collected at longer time scales.

REFERENCES

Bacon, S., Reverdin, G., Rigor, I. G., & Snaith, H. M. (2002). A freshwater jet on the east Greenland shelf. *Journal of Geophysical Research*, 107(C7), 1-16. doi:10.1029/2001JC000935.

Bourke, R. H., Addison, V.G., & Paquette, R. G. (1989). Oceanography of Nares Strait and Northern Baffin Bay in 1986 With Emphasis on Deep and Bottom Water Formation. *Journal of Geophysical Research*, 94(C6), 8289-8302.

Dickson, R., Rudels, B., Dye, S., Karcher, M., Meincke, J., & Yashayaev, I. (2007). Current estimates of freshwater flux through Arctic and subarctic seas. *Progress in Oceanography*, 73, 210-230. doi:10.1016/j.pocean.2006.12.003.

Garvine, R. W. (1999). Penetration of Buoyant Coastal Discharge onto the Continental Shelf: A Numerical Model Experiment. *Journal of Physical Oceanography*, 29(8), 1892-1909.

Gill, A. (1982). *Atmosphere-Ocean Dynamics*. San Diego: Academic Press Inc., 662 pp.

Jakobsson, M., Cherkis, N., Woodward, J., Macnab, R., & Coakley, B. (2000). New grid of Arctic bathymetry aids scientists and mapmakers. *Eos Trans. AGU*, 81(9), 89.

Kundu, P. K. (1976). Ekman Veering Observed near the Ocean Bottom. *Journal of Physical Oceanography*, 6, 238-242.

Leblond, P.H. (1980). On the Surface Circulation in Some Channels of the Canadian Arctic Archipelago. *Arctic*, 33(1), 189-197.

Melling, H. (2000). Exchange of freshwater through the shallow straits of the North American Arctic. In E. L. Lewis et al. (Eds.), *The Freshwater Budget of the Arctic Ocean* (pp. 479-502). Kluwer Academic.

Melling, H., Gratton, Y., & Ingram, G. (2001). Ocean Circulation within the North Water Polynya of Baffin Bay. *Atmosphere-Ocean*, 39(3), 301-325.

Melling, H., Agnew, T. A., Falkner, K. K., Greenberg, D. A., Lee, C. M., Münchow, A., Petri, B., Prinsenberg, S. J., Samelson, R. M., & Woodgate, R. A. (2008). Freshwater fluxes via Pacific and Arctic outflows across the Canadian polar shelf. In R. R. Dickson, et al. (Eds.), *Arctic-Subarctic Ocean Fluxes* (pp. 193-247). Netherlands: Springer, Dordrecht.

Münchow, A. (2000). Detiding Three-Dimensional Velocity Survey Data in Coastal Waters. *Journal of Atmospheric and Oceanic Technology*, 17, 736-748.

Münchow, A., Melling, H., & Falkner, K. K. (2006). An Observational Estimate of Volume and Freshwater Flux Leaving the Arctic Ocean through Nares Strait. *Journal of Physical Oceanography*, 36, 2025-2041.

Münchow, A., Falkner, K., & Melling, H. (2007). Spatial continuity of measured seawater and tracer fluxes through Nares Strait, a dynamically wide channel bordering the Canadian Archipelago. *Journal of Marine Research*, 65(6), 759-788.

Münchow, A., Falkner, K. & Melling, H. (2011). The Baffin Island and West Greenland Current Systems in Northern Baffin Bay: Synoptic Observations and Climatological Context. *Journal of Physical Oceanography*, in press.

Padman, L., & Erofeeva, S. (2004). A barotropic inverse tidal model for the Arctic Ocean. *Geophysical Research Letters*, 31, L02303. doi:10.1029/2003GL019003.

Pond, S., & Pickard, G. L. (1983). *Introductory Dynamical Oceanography* (2nd ed.). Burlington: Elsevier Butterworth-Heinemann, 329 pp.

Rudels, B. (1986). The outow of polar water through the Arctic Archipelago and the oceanographic conditions in Baffin Bay. *Polar Research*, 4 n.s., 161-180.

Samelson, R. M., Agnew, T., Melling, H., Münchow, A. (2006). Evidence for atmospheric control of sea-ice motion through Nares Strait. *Geophysical Research Letters*, 33, L02506. doi:10.1029/2005GL025016.

Simpson, J. H., Mitchelson-Jacob, E. G., & Hill, A. E. (1990). Flow structure in a channel from an acoustic Doppler current proler. *Continental Shelf Research*, 10, 589-603.

Smith, W. H. F., & Wessel, P. (1990). Gridding with continuous curvature splines in tension. *Geophysics*, 55(3), 293-305.

Sokal, R. R., & Rohlf, F. J. (1981) *Biometry*. San Francisco: W.H. Freeman and Company, 859 pp.